SPECTROSCOPICAL ANALYSIS OF MECHANO-CHEMICALLY

ACTIVATED SURFACES

A Dissertation

by

RODRIGO ALEJANDRO COOPER

Submitted to the Office of Graduate Studies of
Texas A&M University
in partial fulfillment of the requirements for the degree of

DOCTOR OF PHILOSOPHY

August 2011

Major Subject: Mechanical Engineering

SPECTROSCOPICAL ANALYSIS OF MECHANO-CHEMICALLY

ACTIVATED SURFACES

A Dissertation

by

RODRIGO ALEJANDRO COOPER

Submitted to the Office of Graduate Studies of
Texas A&M University
in partial fulfillment of the requirements for the degree of

DOCTOR OF PHILOSOPHY

Approved by:

Chair of Committee,	Hong Liang
Committee Members,	Christian Schwartz
	Karl Hartwig
	Alexei Sokolov
Head of Department,	Jerald Caton

August 2011

Major Subject: Mechanical Engineering

ABSTRACT

Spectroscopical Analysis of Mechano-chemically Activated Surfaces. (August 2011)

Rodrigo Alejandro Cooper, B.S. Texas A&M University;

M.S. Texas A&M University

Chair of Advisory Committee: Dr. Hong Liang

Mechano-chemical activation is fundamentally different from chemical activation in that energy is added to alter the state of bond energy instead of exciting electrons to produce a chemical reaction. Mechano-chemical activation has demonstrated to alter the chemical reaction and rates. There remains no development of a model to quantify the changes in reactions due to mechano-chemical activation.

This research aimed in expanding our understanding of the influence of mechano-chemical activation methods. The dynamics and kinetics of mechano-chemically activated surfaces were studied using x-ray spectroscopy methods. Mechano-chemical interactions can be quantified through the study of electron energies.

X-ray spectroscopy is a useful method of analyzing and quantifying electron energy states. X-ray absorbance was used to study the valence state electron shells of iron undergone activation through sliding friction of naturally produced wax. *In-situ* x-ray photoemission spectroscopy was employed to characterize instantaneously single crystal tantalum samples of each principal crystallographic orientation during oxidation.

Sliding friction of the naturally produced wax resulted in a reduction in the binding energy of the iron 2p electrons by approximately one electron-volt. This reduction in binding energy is attributed to ferrocene, which is an organo-metallic alloy, $Fe(C_5H_5)_2$.

Mechanical strain of the crystal lattices of tantalum resulted in altered activation energies. Activation energy increased with the application of lattice strain. At increasing strain, oxide properties became more dependent on the lattice strain than the crystal orientation and temperature. A model system was developed incorporating mechanical strain into the prediction of activation energy and rates.

DEDICATION

To my parents and sister for making me stubborn

To my advisor for making me persistent

To my Aggie family for making me strong

To all those I have met along the way for making me proud

ACKNOWLEDGEMENTS

Finally, I would like to recognize the support from my family who has stood by every hard decision I have had to make in order to progress professionally. Their encouragement has never fallen short when most needed.

TABLE OF CONTENTS

LIST OF FIGURES

LIST OF TABLES

Page

CHAPTER I

INTRODUCTION

In the current research, x-ray spectroscopic analyses were performed to expand the understanding of mechano-chemical activation of reactive materials. Mechano-chemical activation of metals in a lubrication regime and in gaseous environment are investigated to determine the factors and effects of different parameters used in the mechanical activation.

1.1. X-ray spectroscopy

All elements in nature are composed of a neutron and an electron cloud. The structure of the electron cloud is such that every electron has a distinct energy[1-2]. X-ray spectroscopy for crystal structure analysis was first implemented by W.H. Bragg in 1911[3]. Bragg used an high energy electrons as an excitation source and measured the x-ray wavelengths emitted from various samples. X-ray diffraction methods had been used prior to Bragg's studies, but these methods described spatial distributions whereas spectroscopy was the first to provide energy distributions.

Since the energy of an electron is dependent on the neutron of the atom and forces exerted by neighboring atoms, spectroscopy is a functional tool in determining not only the elements present, but the physical and chemical properties of the atoms as well. All chemical and physical properties rely on this energy distribution, making x-ray spectroscopy an important tool for materials studies.

This thesis follows the style of Journal of Applied Physics.

X-ray spectroscopy is a very sensitive to the environment of the atoms[4]. This allows for specific bonds to be determined using different methods of spectroscopic analysis. In x-ray emission spectroscopy, a hole is created by the ejection of an electron in the core shells. An electron from a higher energy shell subsequently drops to fill this hole and emits energy in the form of x-rays[5]. Adsorption spectroscopy occurs by the ejection of a core shell electron to the first empty level of the conduction and photoemission spectroscopy ejects the electron completely out of the atom.

Any slight perturbation in the atomic structure is detectable[6]. Since chemical reactions require the transfer of electrons, x-ray spectroscopy provides a means of monitoring how a reaction occurs. X-ray spectroscopy is limited to a few tens of angstroms from the surface, making it strictly a surface analyzing method[7].

A detailed description of x-ray adsorption, x-ray diffraction, and x-ray photoemission will be provided in Chapter III of this thesis to provide the reader with sufficient knowledge as to the workings of each.

1.2. Activation

In a chemical reaction, molecules need to overcome a minimum energy barrier in order to transform into its products. This energy barrier is referred to as the activation energy. This energy is typically provided by external sources which activate atoms in a material.

Activation of a material occurs when surface electrons are excited and forced to react with their environment due to an outside stimulus. The ability, ease, and

availability of these excited electrons prescribe particular reactions and reaction rates. Three methods of activation have been widely studies and modeled: thermal, photo, and electrical. A brief explanation of each will be provided in the following section. A more recently studied activation method, mechano-chemical activation, will be presented last, with more detail and present previous studies that have witnessed the effects of mechano-chemical activation.

1.2.1. Chemical activation methods

Chemical activation methods are those methods in which the electron structure is altered and the reaction or products become affected. There are three common methods that have been widely studied and will be presented in the following section.

1.2.1.1. Thermal

Thermal activation deals with the study of how electrons can be excited from one state to another by the input of energy in the form of heat[8]. In the simplest form, a reaction can occur in which the potential of a molecule can be altered by heat, particularly for metastable states and nonequilibrium systems[9-10]. Thermo-activation is commonly seen in transport, catalysis, and diffusion systems[11].

Thermal activation has been reported to alter the product of novel processes where all other variants are fixed[12]. Surface electrons bound in a deep potential well can be excited to a point of desorption from the surface[13].

In other studies, thermal activation is seen to force core electrons from their ground states to higher energy shells. When the thermal energy was removed, the

electrons returned to their ground states while releasing energy in the form of luminescence[14]. Depending on the extent of thermal energy, electrons could be forced into conduction bands with the addition of thermal energy and return to an energy state higher than their original state upon removal of the thermal energy[15].

Synthesis of particular nanostructures is affected by thermal activation. It is important to maintain control of size and composition of nanoparticles for use as catalysts. One way to have such control is to control the inter-particle and surface access properties of the nanoparticles[16]. By doing so, activation of the core electrons can be finely controlled to allow only certain processes to occur[17].

1.2.1.2. Photon

Photo-activation results in the excitation of electrons by photon adsorption[18]. In this scenario, a photon irradiates an atom exciting an electron to a point where this is ejected from its orbital. Depending on the photon energy, the ejected electron can achieve a higher energy orbital or be completely ejected from the electron cloud.

Photo-activation is particularly important in the synthesis of nanoparticles with a high control on size distribution[19]. By avoiding complex chemical reduction processes which depended on various factors, photo-synthesis of nanowires resulted in a fast production process with a small size deviation. In one particular experiment, it was found that Pd nanowires could only be produced with the irradiation of UV light and the size was dependent to the light dosage[20]. Similarly, gold nanoparticle synthesis is defined in shape and size by the intensity and exposure time of UV light[21-22].

In studies with Mg, it was shown that O_2 adsorption could be enhanced by photo-activation of the Mg particles. The rate of adsorption and total amount was determined and controlled by exposure to light and intensity.

1.2.1.3. Electric

Electro-activation is the foundation of electrochemistry in which energy is exchanged in the form of electron transfer. This is the foundation of the field of electro-chemistry and the application of many industrial processes. Electrons are transferred or released due to the application of an external voltage on the active sample.

Electronic state alterations via an applied voltage result in changes in oxidation of metals. Such application has been studied for electro-chemical mechanical polishing[23]. The oxidized material was removed by abrasives exposing the bare metal. An applied voltage to the sample altered the chemical state of the surface causing it to change the oxidized product. Different oxides have different mechanical properties[24]. Having control of which oxides to produce allowed for manipulation of the wear[25].

Kinetic reactions have also been seen to be altered by the application of a potential to alumina causing it to increase the adsorption rate of fluoride[26]. This reaction can be controlled by altering the charge state of the particles through an electric field. It was also found that application of an applied electric field increased the total adsorption of granular carbon.

Electrical activation also occurs in polymers by altering the phase and structure of the polymer chains[27-28]. The crystal structure, phase, and morphology where altered

with the application of an electrical potential across the surfaces of polyvinylidene difluoride (PVDF)[29-30]. The charge differential forced a dipole alignment in the piezoelectric material increasing the concentration of β-phase which degenerated with the release of the potential[31].

1.2.2. Physical activation

Physical activation is a relatively recent discovery of altering the reactivity of a substance. The term "mechanical activation" was first coined in 1942 by Smekal[32]. Unlike the chemical activation methods, mechanical activation does not excite electrons from the reacting surface to higher energy orbitals. Mechanical activation functions primarily by stressing the chemical bonds thus influencing the reaction.

Reactions resulting from a mechano-chemically activated transformation are determined by the extent of structural disorder, the mobility of atoms, and the relaxation of stressed bonds with the liberation of stored energy[33]. Mechano-chemical activation affects the chemisorptions, ionization of structural defects, the production of non-equilibrium states, alteration of the diffusion controlled reaction, amongst many more.

Mechano-chemical activation processes introduce internal energy to surface atoms. This added energy facilitates and reduces the energy required to overcome the activation energy[34]. As a reaction follows, the added energy and reaction rearrange the structure[35].

Sources of mechanical activation will be discussed in a later section, but first, a brief description of applications of mechano-chemical activation will be presented in the next sections.

1.2.2.1. Application of mechano-chemical activation

1.2.2.1.1. Nano-synthesis

Though mechanical activation does not alter the electronic structure of atoms and molecules, the added energy through mechanical force is capable of producing scenarios leading to chemical reactions.

An example of such chemical reaction due to mechanical force is the synthesis of silver nanochains[36]. Sliding silver nanoparticles against each other in 18-crown ether-6 introduced sufficient energy in the covalent bonds of the crown ether to break its bonds as seen in Figure 1. The oxygen terminated bonds that result from such rip react with Ag ions forming the nanochains, as seen in Figure 2. The length of the chains is determined by the friction energy and duration of the sliding motion.
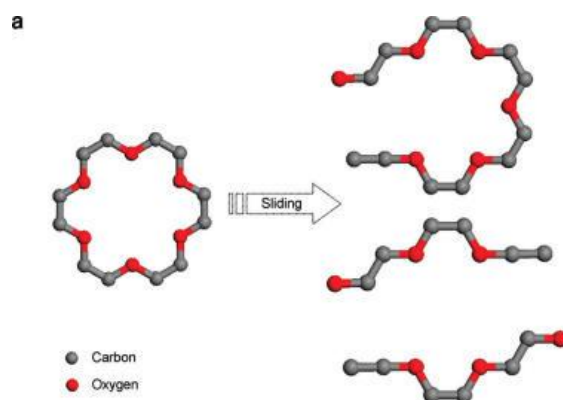
Figure 1. Sliding friction force split the covalent bonds in a crown ether
ring
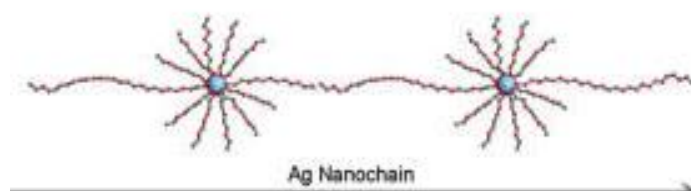
Figure 2. Broken crown ether rings react with Ag ions to form chains

1.2.2.1.2. Biasing reaction pathways

Thermoplastic polymers are known to change properties during plastic

deformation under an applied stress. At the macroscopic level, deformation is evident by

a change in cross-sectional area and length of a specimen. At the microscopic level,

polymer chains undergo a complex transition due to chain sliding and rupturing[37]. In

deformed thermoplastics, deformation has been shown to increase crosslinking and

entanglements, as shown in Figure 3. The degree of crosslinking and entanglements is

known to have a direct relationship to the chemical and mechanical properties of the

polymer[38].
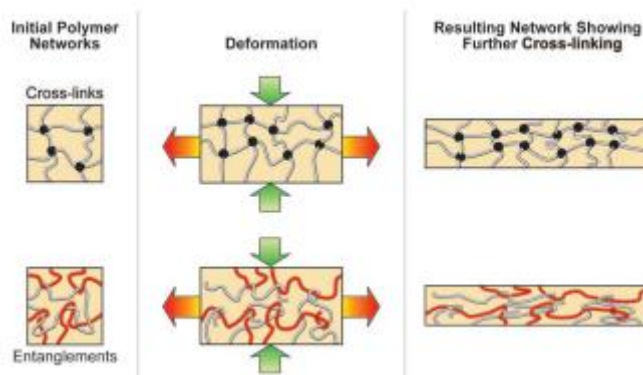
Figure 3. Strain of a thermoplastic polymer increases crosslinking and
entanglements[39]

1.2.3. Mechano-chemical activation

1.2.3.1. Activation

Mechano-chemical activation occurs through mechanical energy input in the

form of friction and deformation. There are many sources and forms of providing

deformation to a sample. For the purpose of this study, we will focus on lattice

deformation.

For many applications in the microelectronics industry, depositing metal coatings

or films on the surface of other substrates is a common practice. The deposition of such

films produces an intrinsic stress on the film dependent on the film thickness[40-41]. This

stress is associated with a lattice mismatch from the epitaxial growth of one metal on top

of another material with dislike lattice parameters[42]. The ensuing lattice mismatch

provides a stress on the deposited metal lattices[43]. The mismatch can induce a stress on

the lattices of the deposited material to the point of developing surface features, as

shown in Figure 4 and Figure 5. In the figures, lattice mismatch created regions of high

stress that only by taking novel geometry could be dissipated.
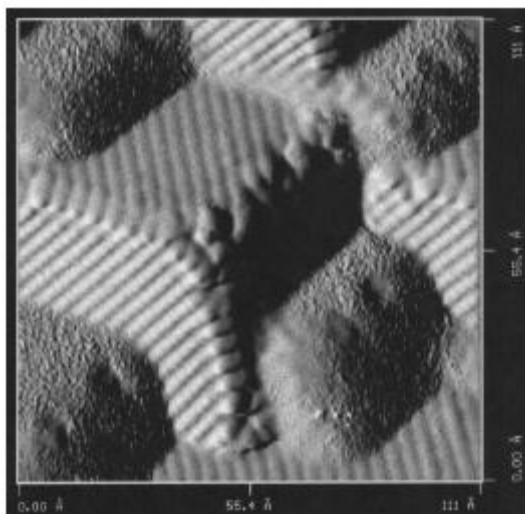
Figure 4. Lattice mismatch of Pd film deposited on W(111) creates a
textured surface[44]
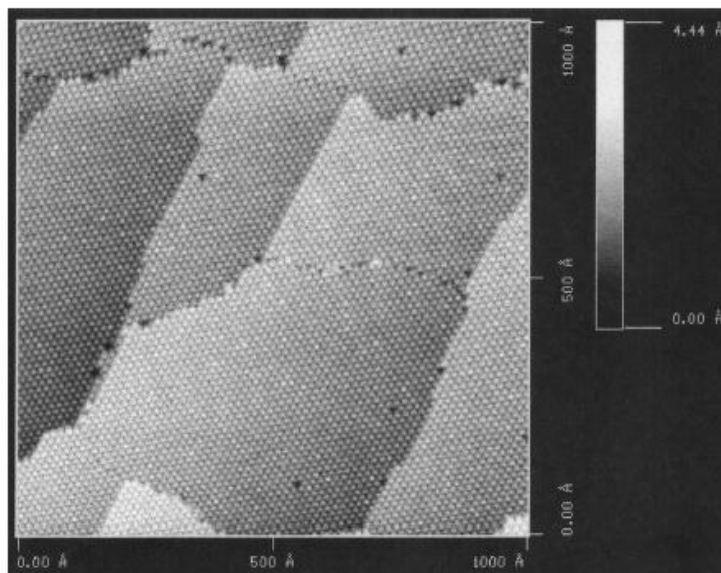
Figure 5. Sulfur deposited on W(111) creates high stress regions of
terraces to reduce stress[44]

Similarly, hydrogen adsorption on Si(100) is seen to change its adsorption

mechanisms due to a straining of the substrate lattices[45]. An unstressed substrate

produces a uniform monohydride surface, as seen on Figure 6-a. An applied strain on the

substrate lattices develops a surface of alternating monohydride and dyhydride, as seen

in image b.
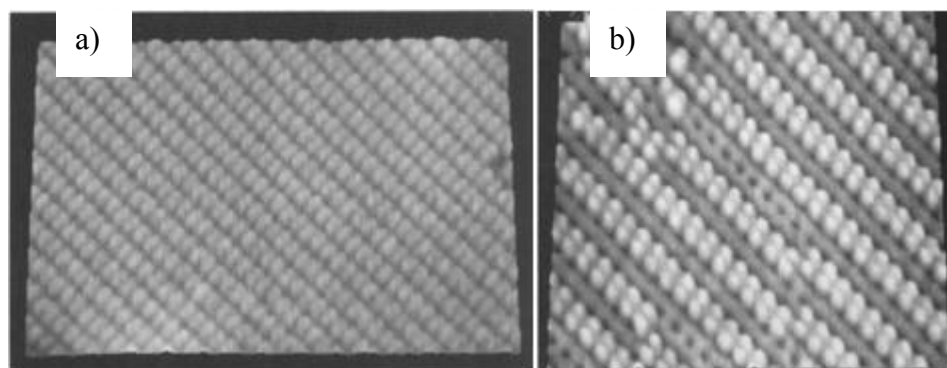
Figure 6. Surface strain on Si(100) changes the mechanism of hydrogen adsorption producing an alternating monohydride and dihydride surface[45]

1.2.3.2. Effects of activation

The lattice mismatch introduces a mechanical stress on the deposited material. This mechanical stress is the source of the mechanical activation and is known to alter the chemical reaction of the exposed surface.

It has been widely investigated that lattices which exhibit some form of strain have an altered adsorption energy[46]. As seen in Figure 7, applying different strains to Pd(100) has produces different percent adsorption of CO. It is seen that a small strain is capable of producing a large change in the equilibrium pressure.
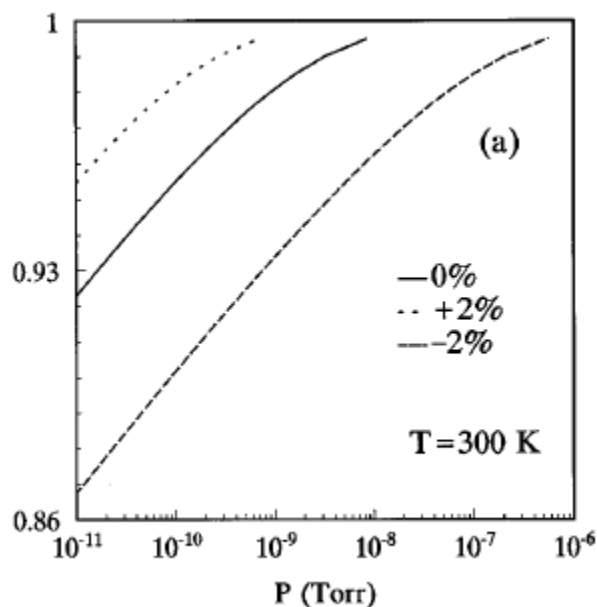
Figure 7. Strain on Pd(100) changes the percent adsorption of CO[47]

The energy of adsorption and dissociation of CO on Ru(111) is shown in Figure 8. The figures support the previous figure in that a compressed sample would have a higher energy of adsorption. A compressed lattice site would not be as readily available to react as a lattice site in tension. This is also supported by Figure 9 in which it is seen that oxygen is adsorbed firstly in the tensile regions of a deformed site on Ru(111). The final location for oxygen to be adsorbed is the location with compressed lattice sites.
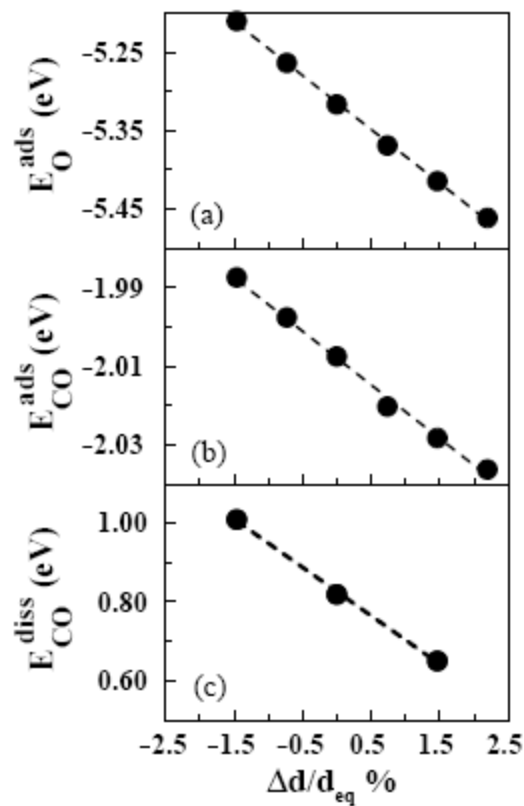
Figure 8. Energy of adsorption and dissociation is related to lattice strain as shown in this example of CO on Ru(111) [42]
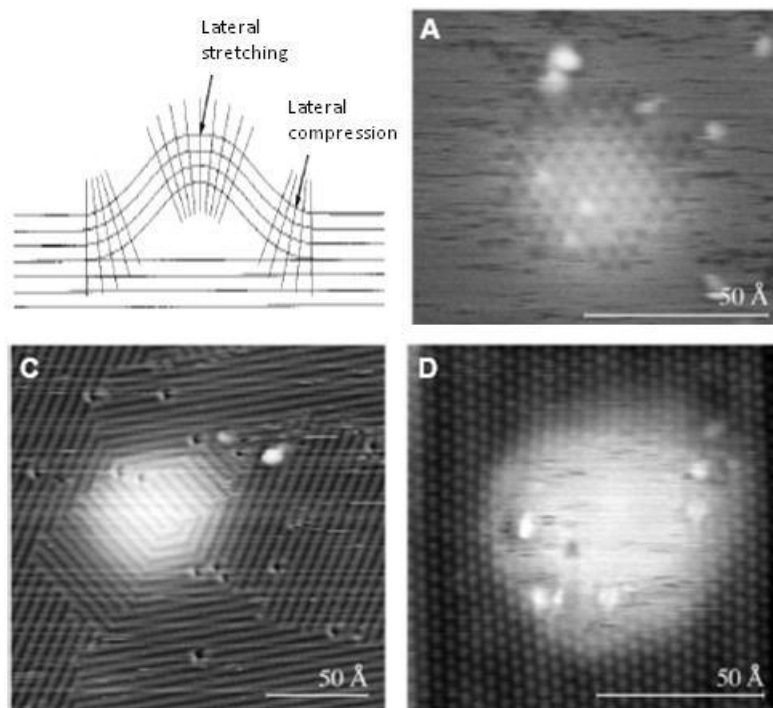
Figure 9. Adsorption of oxygen on Ru(111) begins in the stretched
lattice sites, followed by neutral sites, and finally at the compressed
lattice sites[48]

1.3. Tantalum

Tantalum pentoxide is becoming an increasingly important dielectric material for
capacitors, photonic optics, and dynamic random access memories (DRAM), amongst
other uses [49-52]. Its increasing importance to the development of microelectronics is
evident by an increase in papers published in the last 20 years[52], as seen in Figure 10.
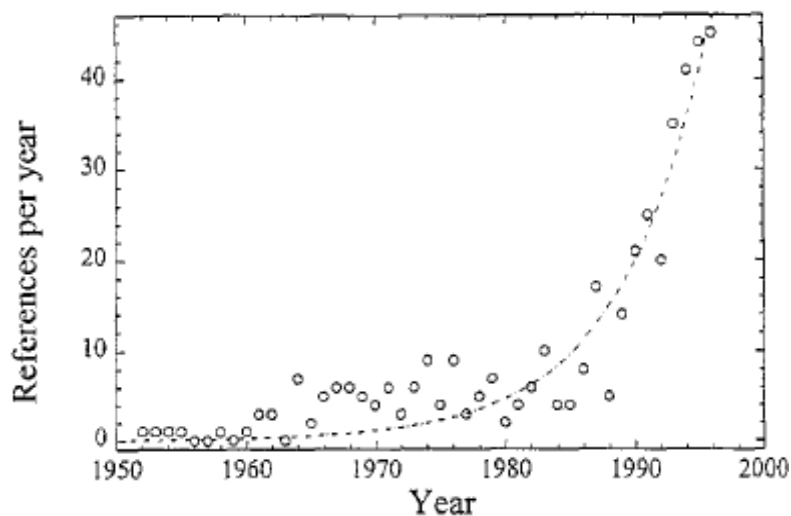
Figure 10. Number of references related to tantalum pentoxide for the
last 60 years[52]

As the microelectronics decrease in size and increase in density, challenges arise

due to electron leakage between the copper interconnects and the silicon substrate[51]. In

order to continue decreasing feature dimensions, materials with a higher dielectric

constant are needed that would reduce electron leakage[53] by functioning as dielectric

barriers as shown in Figure 11. The list of potential materials for dielectric barriers

include TiO, PbO3, TiO3, and tantalum pentoxide[54]. Current deposition methods for the

DRAM industry make tantalum pentoxide an ideal candidate for dielectric materials due

to its thermal stability and ease of incorporating with current deposition methods[51,55].
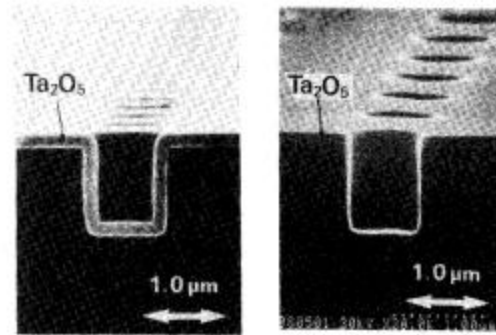
Figure 11. Tantalum as a dielectric barrier for DRAM applications[56]

During manufacturing, the most common process for surface planarization of tantalum is chemical-mechanical polishing (CMP) and electrochemical-mechanical polishing (ECMP) [25]. Improvements in tantalum CMP and ECMP have focused on three major constituents: pad, abrasive, and chemical environment[57]. Many studies have focused on the effect of the abrasive silica particle size used in the polishing slurry[58]. It has been proposed that the material removal rate and surface finish of tantalum is affected by the specific surface area of the particles due to larger chemical bonding[59]. Changing the chemistry, i.e., oxidizers and pH, of the slurry alters the surface chemistry of tantalum thus changing the properties affecting the material removal rate[60].

It has been shown that surface stresses can affect the tantalum oxidation composition [61]. It was also shown that the activation energy and the kinetics of oxidation can be altered by the energy exerted on during polishing by the normal load on tantalum[62] and revisions to the Arrhenius equation of activation were provided to account for such energy.

There have been few studies relating the resultant surface stress to the oxidation kinetics [42,45,48,63]. In the present study, we aim at studying the effect of residual surface stress on the oxidation of tantalum. We eliminate the three common factors of polishing, pad, particle, environment, to understand the fundamental effect of the stress on the chemical response. We employ an ambient-pressure x-ray photoemission spectroscopy (AP-XPS) [64-66] capable of operating at near ambient pressures. We also prepare a model to predict and explain the effects of mechanically induced stress on the resulting reaction.

1.4. Naturally produced lubricant

Nature has its unique ways to deal with harsh environment and to maintain cleanliness of surfaces[67]. Insects have developed the ability to produce a complex wax that maintains their surface clean from debris and contaminants[71]. There exist many sources of naturally produced wax, or bio-wax, including a wide range of insects and several plants[68].

Amongst one of the top producers of wax is the American cockroach, *Periplaneta americana*. The American cockroach has specially developed glands, shown in Figure12, to produce its own biowax which it secretes to completely cover the entire roach.
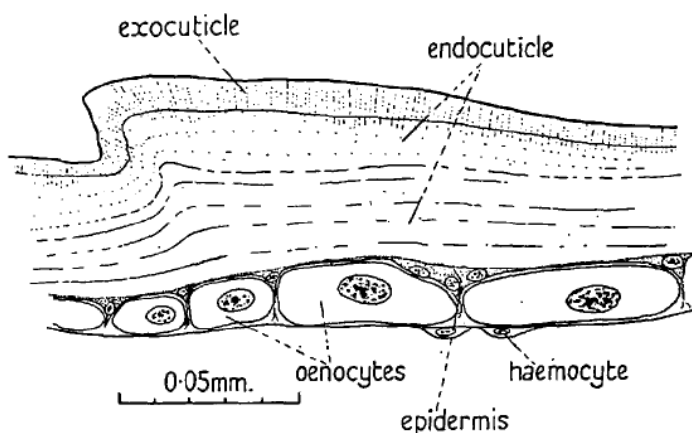
Figure 12. Cross section of cuticle of *P. Americana*

Aside from maintaining a clean surface, this roach uses its bio-wax as an internal humidity controller[69-73]. The wax is also used as a scent signal for other roaches [74]. The secretion has been identified as a wax composed of even-number primary alcohols and odd-number paraffin from C_{25} to C_{37} [68]. The wax is composed primarily of a mixture of hard waxes closer to the cuticle and a thin layer of liquid waxes [70]. Previous works have estimated the thickness of the wax layer of 0.11μm throughout the entire body [75] under the assumption of equal distribution of the wax throughout the cuticle.

Of particular interest is the fact that biowaxes tend to have longer carbon chains than synthetic greases, as shown in Table 1. The biowax is also produced from varying carbon chains as opposed to a singular carbon chain for synthetic greases. Furthermore, the American cockroach wax is known to be able to support a high pressure load, as shown in Figure 13, before collapsing and splitting the molecular chains.

Table 1. Molecular weights of various waxes, natural and synthetic[70]

Material	% volatile material	Molecular weight from freezing-point	Molecular weight of volatile components	Equivalent carbon chain
Hard cockroach wax (see p. 522)	—	420–255	—	C 27–C 29
Stearic acid (M.W. 284)	—	265–280	—	C 18
Beeswax	—	360–390	—	C 25–C 27
Vaporized grease	—	295–350	—	C 22–C 25
Whole grease Sample A	41	315	139	C 10
B	37	345	184	C 13
C	29	355	148	C 11
D	27	370	176	C 12
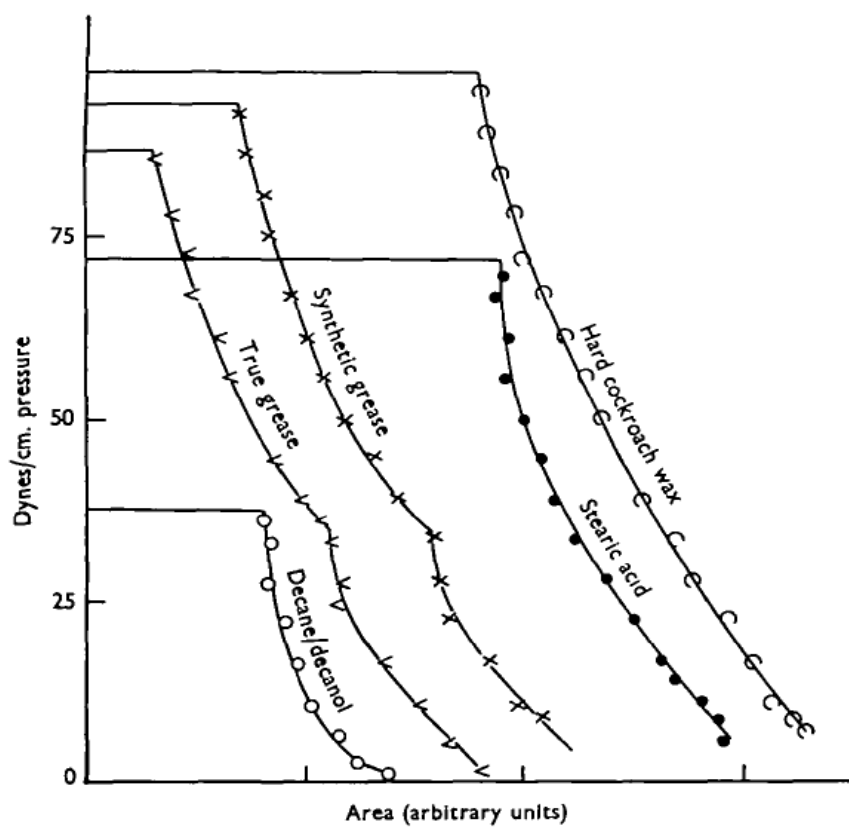
Figure 13. Cockroach wax can tolerate pressures higher than many synthetic greases before collapsing and destroying its molecular chains[70]

As micro-electromechanical systems (MEMS) and nano-electromechanical systems (NEMS) become more complex and smaller, interacting mechanisms experience larger effects from stiction and friction[76-77], not to mention contaminants[78]. Scientists and engineers have tried to learn from nature in order to make effective cleaning products for MEMS and NEMS devices.. In microelectronics industry, manufacturing processes require fabrication in a clean room environment with additional steps in the post-process cleaning [79-80]. Surface cleaning remains to be the challenge due to difficulty, cost, and environments.

Biowaxes are studied here for potential use as a MEMS/NEMS lubricant. They are considered since they can bear such high loads without collapsing. At smaller scales, even small loads can exert a large pressure due to the infinitesimally small contact area.

1.5. Summary

A basic introduction to spectroscopy and its abilities was presented. Spectroscopic analysis is capable of providing information on the electronic structure of atoms. This method is sensitive to perturbations to the electronic state of atoms. Since chemical reactions require the transfer of electrons and formation of different bonds, x-ray spectroscopy provides a reliable method of monitoring reactions at the atomic scale.

In this chapter, basic understanding of methods of activation and the effects of mechano-chemical activation were presented. Effects of strained lattices were introduced, though theory has not developed to provide a measurable prediction as to the reaction under these conditions.

CHAPTER II

MOTIVATION AND OBJECTIVES

As discussed in Chapter I, studies have been performed to have a thorough understanding into the effects and causes of chemical activation via thermo, photon, and electrical activation. In contrast, there is not sufficient understanding as to the physical activation methods described in Chapter I: mechano-chemical activation.

2.1. Objectives

In this research, we will aim at achieving a series of objectives that would expand our knowledge of mechano-chemical activation. The objectives are listed below.

1. Identification or generation of mechanically strained sample materials as model systems for synergetic studies.

2. Quantitative characterization of mechano- chemical interactions.

3. Obtaining understanding in dynamics of mechano-activated surfaces.

4. Obtaining understanding in kinetics of mechano-activated surfaces.

2.2. Outcomes

These objectives will be met by studying reactions of mechano-activated samples by x-ray spectral analysis, discussed more in Chapter III. *In-situ* characterization of a mechano-chemical interaction of single crystal tantalum will be performed on strained samples. These studies shall give an insight as to the dynamic and kinetic processes and alterations caused by the addition of mechanical energy to the crystal lattices.

By studying the dynamic effects of oxidation of mechano-chemically activated samples, we will propose a model to incorporate such activation energy for the calculation of activation energy of the system. By creating such a model, contributions of stress and strain on the lattices will be able to be quantified in order to tailor future reactions.

2.3. Dissertation structure

This dissertation is presented with a brief introduction in activation and effects of mechano-chemical activation as Chapter I. A list of motivations and objectives will be presented in Chapter II. A description of the spectral analysis performed to evaluate the mechano-chemical activation of different materials will be presented in Chapter III. Detailed discussion of mechano-chemically activated studies and spectral analysis will be presented in Chapters IV, V, and VI. Finally, conclusions and future recommendations will be presented in Chapter VII.

CHAPTER III

MATERIALS AND METHODS

The objective of this chapter is to familiarize the reader on the samples, testing, and characterization techniques employed for these studies. The aim of this research is to investigate lubricated surfaces of metallic materials. The lubrication focuses on nature-inspired wax and the substrate on tantalum. Sample description and preparation will be divided into two parts; one for bio-waxes and another for tantalum samples. Finally, a brief introduction into the theory of the characterization methods utilized and analysis will be explained in the third section.

3.1. Bio-wax preparation

Testing and characterization of naturally occurring waxes were performed on the American cockroach, *Periplaneta americana* due to their ease of breeding and handling. Mechanical activation of the wax was performed on bulk substrates. The process for such tests is presented in the following sections.

3.1.1. Collection of bio-wax

In this experiment, only laboratory bred and grown roaches were used to avoid environmental variables that may produce minute changes in the constitution of the wax. The roaches were maintained in plastic containers, approximately 42x30x15 cm in size, as shown in Figure 14. The boxes were stocked with wood chips to control moisture and filter waste. Each box contained approximately 100 roaches, sufficient to maintain a

healthy population without overcrowding. Dog food (Puppy Chow, Inc) and water were added *ad libitum*. All insects used in this experiment were adults.

The roaches were kept in an environment-controlled room set to mimic ideal living conditions for the roaches. The room was maintained at 30°C with 70-80% relative humidity levels. Twelve hour light and dark cycles were controlled to replicate the roaches' diurnal habits. Dead roaches are removed promptly after discovery to prevent diseases from spreading to the colonies.

Figure 14. Roach colony with shelter, food, water, and wood chips.
Each colony consisted of approximately 100 roaches of mixed gender
and age

The thickness of the existing layer is still disputed amongst researchers, but a general consensus agrees it to be within tens of microns with minor variations depending on the anatomical location [71,75,81]. Studies have shown that the dorsal and ventral sections, identified in Figure 15, of the abdomen differ in purposes. The wax thickness varies in as appropriate for its function[82-83]. While for most of the body the wax serves as a waterproofing mechanism to control transpiration or as a carrier for sex pheromones[72-73], studies have shown that the ventral section requires a thicker amount of wax due to its constant rubbing with the ground [84].

Figure 15. Wax coating thickness of a cockroach varies according to
the anatomical location and purpose at that particular location

The composition of most naturally produced waxes, either by plants or insects, comprises of long chain paraffins, alcohols, and small quantities of esters, as shown in

Table 2[68,70,73-74,85], The wax on the cuticle of the American cockroach soluble to hexane, methanol, and chloroform.

Table 2. Composition of most naturally produced waxes is composed
of even-numbered paraffins and alcohols

Chain Length	Paraffin	M.W.	B.P (°C)	Alcohol	M.W.	B.P (°C)
C4	Butane	58	Gas	Butyl	74	117
C6	Hexane	86	69	Hexyl	102	157
C8	Octane	114	125	Octyl	130	195
C10	Decane	142	174	Decyl	158	231
C12	Dodecane	170	214	Dodecyl	186	solid
C14	Tetradecane	198	5			

A 'bath' of approximately 200mL of methanol (Sigma Aldrich, 99.8% wt.) was prepared in a glass receptacle where the roaches were dipped and swirled for ten seconds, as seen in Figure 16. Prior to bathing, the roaches were sedated with CO_2 gas (Botco Inc., 99.8% purity) to ease handling and allow time for inspection. Roaches were inspected to verify they had a healthy luster, indicating a good coating of wax, and ensure no debris or visible contaminants were present on the surface. Sedation of the roach also eliminated bodily fluids from being secreted by the roach during bathing.

Figure 16. Roach wax removal methanol "bath" captures approximately
two to four microliters of wax

Approximately one hundred roaches were bathed together at a time. The bath

solution was then passed through a wire mesh colander to remove the roaches.

Inspection of the roaches revealed a matte surface indicating a thorough removal of the

wax. Removal of the wax resulted in immediate death of the roaches. A total of five to

seven similar baths were made and mixed after having the roaches filtered.

The solution was left to evaporate in a fume hood at room temperature leaving behind

only the roach wax. Depending on the average age, size, and gender of the group, the

solution yielded approximately 2-4mL of the biological roach wax. The remaining

residue is expected to be pure cockroach wax. The wax is a yellow-brown substance

with a noticeable smell of cockroach.

3.1.2. Sample preparation

The wax collected deposited at the bottom of the glass beaker after the methanol evaporated. The final consistency of the wax was similar to toothpaste but with a yellow-brown hue. To perform proper testing, a uniform coating on a substrate was needed. A method of drop-casting was performed to obtain such uniform thickness. However, to achieve this, the wax needed to be reprocessed prior to any testing and characterization.

To get a proper and uniform coating using the drop cast method, the wax needed to be dissolved into a less viscous substance. In order to do this, the wax was removed from the beaker by scrapping it with a stainless steel spatula and transferred to a 20mL glass vial. Approximately 2-4 mL were collected in the vial and diluted with 20 mL of methanol. The vial was shaken vigorously for a minute prior to depositing onto the substrates. A pipette was used to apply 100μL of the wax-methanol solution to the substrates. The sample was then allowed to dry in a fume hood and the process was repeated until a visible coating evident on the sample surface. When the solution on the substrates had fully evaporated, it left behind a thin coating of roach wax. The solution was subsequently reapplied 10 times in the same manner.

The substrates used were stainless steel 316 samples due to their known chemical stability. A brief description is provided in a following section.

3.1.3. Wax tribo-testing

Testing was performed on a CSM tribometer in linear reciprocating mode as seen in Figure 17. Samples described previously coated with the bio-wax and control,

uncoated samples of the same material were tested. The counter-surface was a fixed

6mm alumina bearing to simulate a ball-on-flat condition. The ball displacement was set

at 5mm with a reciprocating frequency of 5Hz. A normal load of 1N was applied on the

pin holding the ball. The test was performed for 400 cycles while collecting friction

force measurements parallel to the reciprocating motion.
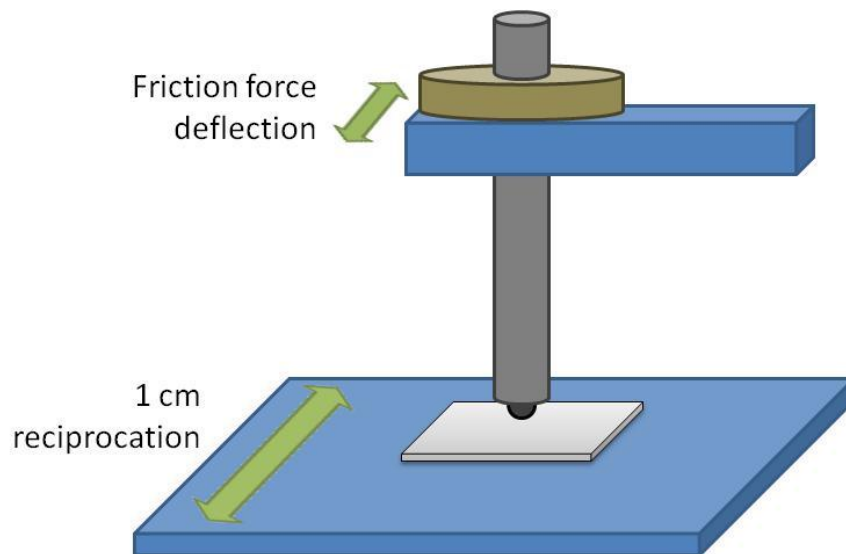
Figure 17. Reciprocating motion with normal load on CSM tribometer
to mechanically activate reaction of bio-wax

3.1.4. Stainless steel substrates

The roach wax for tribology testing was deposited unto stainless steel 316

substrates. The stainless steel substrates were cut to 1"x1" square samples from a ¼"

thick laminate. The samples were polished to a matte finish with a roughness within 2

microns with abrasive pads on an Buehler polisher/grinder machine.

The samples were sonicated in DI water for 15 minutes and rinsed with acetone after polishing to remove all debris and surfactants from the surface. The first wax coating by drop cast method, as described previously, was applied within 15 minutes of the acetone rinse to prevent contaminants from forming on the surface.

3.2. Tantalum samples

3.2.1. Samples

Single crystal tantalum samples are used to study the effects of lattice strain on chemical surface reactions, mainly oxidation reactions. Three pairs of samples were obtained from Goodfellow Co. with 99.99% wt purity. Two samples of each principal crystallographic plane orientation, (100), (110), and (111), were used for this experiment. All six samples were 10mm diameter cylindrical specimens 2mm long.

3.2.2. Preparation

Each crystallographic plane orientation pair consisted of a control sample and an altered sample. The control sample of each orientation underwent thorough chemical-mechanical polishing (CMP) to achieve a mirror finish. Polishing was performed at 40RPM with a 2N normal load in a 1%wt H_2O_2 solution with 0.3%wt alumina abrasive and a polishing pad. No further treatments were performed to the control samples. Crystal orientation and uniformity were performed using an X-ray diffraction (XRD) technique.

One sample of each crystallographic orientation was prepared to produce a relatively small level of strain at the lattices. This group of samples was uniaxially compressed along the cylindrical axis by parallel plate compression. A tensile/compression machine (Instron 4206) was employed to provide the 16GPa of compressive pressure to induce plastic deformation on the sample. The final dimensions of the samples are listed in Table 3. Compressed samples were subsequently polished with the same conditions as the control samples and characterized by XRD technique.

Table 3. Sample dimensions of original and compressed samples

	Diameter (mm)	Height (mm)
Original Samples	10.000	2.000
Compressed (100)	14.439	0.959
Compressed (110)	13.863	1.041
Compressed (111)	13.154	1.156

3.3. Testing

3.3.1. Nanoindentation

Nanoindentation tests were performed to gain an insight as to the surface properties of the samples. An MTS Nanoindenter XP is utilized due to its oscillating loading ability which is capable of providing material properties such as, but not limited to hardness and modulus of elasticity[86].

A Berkovich tip is utilized to as the indenter. Nanoindentation provides a measure of the load on the Berkovich tip, *P*, as a function of penetration depth, *h*, as seen in Figure 18. As the load increases and penetrates the sample, the tip induces elastic deformation followed by plastic deformation. The loading is typically exponential as shown in the graph due to an increase in contact area between the tip and sample.
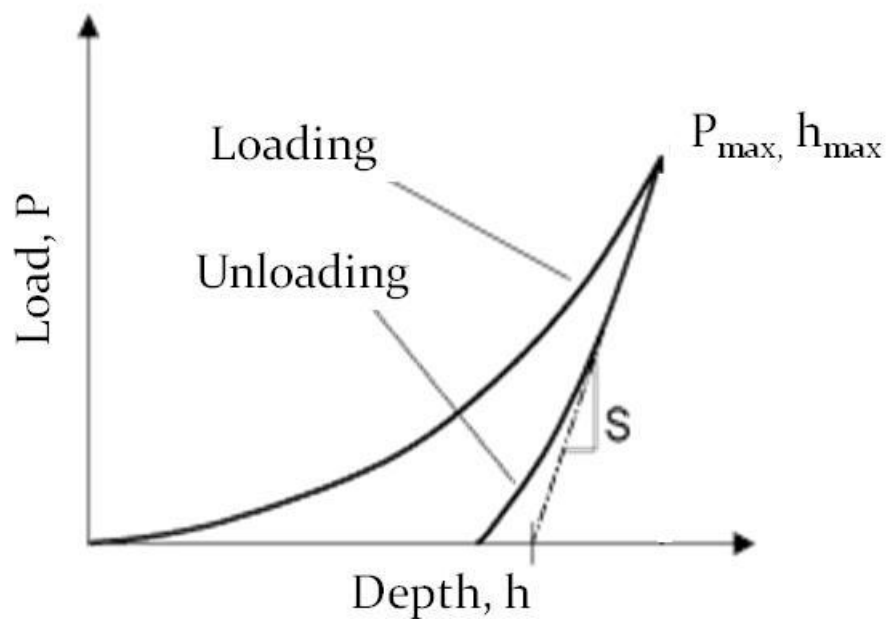
Figure 18. Nanoindentation studies are performed by measuring the
load with respect to penetration depth

The hardness of a material, H, can be calculated by a measurement of the maximum load and penetration depth, as defined below.

$$H = \frac{P_{max}}{24.5 h_{max}} \qquad (1)$$

The modulus of elasticity is calculated by the following equation.

$$E_r = S \frac{1}{h_{max}\beta} \sqrt{\frac{\pi}{24.5}}$$ (2)

where S is the contact stiffness during the initial unloading regimen, shown on the plot.

A geometry factor, β, of 1.034 is used for tests with the Berkovich tip. E_r is the reduced

modulus of the sample and equipment combined. By careful calibration and

measurements of the equipment, this can be used to obtain the modulus of elasticity of

the sample by the following equation.

$$\frac{1}{E_r} = \left(\frac{1-v_{sample}^2}{E_{sample}}\right) + \left(\frac{1-v_{indenter}^2}{E_{indenter}}\right)$$ (3)

By performing continuous and escalating loading and unloading segments, the

hardness and modulus of elasticity can be calculated throughout the depth of an indent.

3.3.2. Evaluation of lattice strain

Crystallographic assessment of the initial samples was performed by X-ray

diffraction (XRD) method on a Bruker D-8 Bragg with a wavelength of λ=1.542Å. XRD

is a common technique for powder diffraction, phase identification, crystal orientation

and quantification, and residual stress measurements [87-89].

XRD functions by directing a soft x-ray onto a sample. The x-rays are reflected

and scattered by the surface layers, as seen in Figure 19. The incident x-rays, shown in

blue, penetrate the top surface and reflect the x-rays, in red.
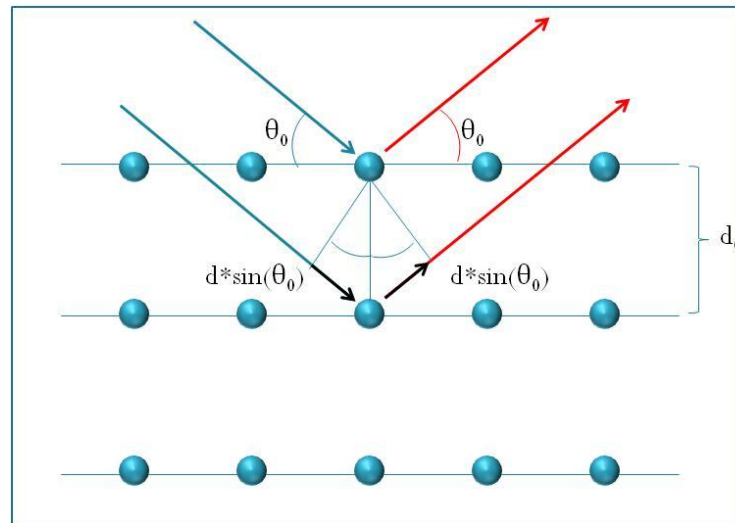
Figure 19. Method of XRD accounts for differences in time-of-flight of
reflected x-rays from different planes parallel to the surface

The reflected x-rays will have a phase lag due to different times-of-flight as their

path distance is varied with penetration depth. The emitted x-rays will either be in phase

or out of phase and cause either constructive or destructive interference, as seen in

Figure 20.
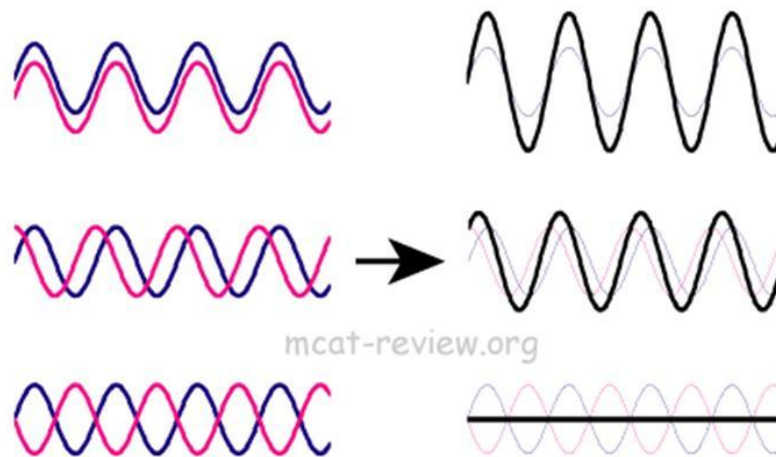
Figure 20. The plane distance of a crystal will reflect x-rays with a lag
causing it to create constructive or destructive interference

As the incident angle is changed, the time-of-flight for the subsequently deeper

planes changes until an angle is obtained where all emitted x-rays are in phase and

provide a strong signal. The plane separation can be calculated using equation 1. A

known incident wavelength, λ, at a known incident angle, θ, can be used to calculate the

plane separation, d. For single crystal materials, such as the tantalum species used in this

experiment, the indicated crystal orientation is parallel to the surface, thus only one

value of θ will obtain constructive interference.

$$\lambda = 2 * d \sin(\theta) \qquad (4)$$

Crystal lattice strain can be introduced when samples undergo chemical, thermal,

or mechanical alterations. XRD technique is useful for quantifying lattice strain due to

the residual stress. Using Hooke's law, the stress can be calculated from the strain

distribution [90]. As the lattices are strained, the planar separation is equally changed and resulting in a different value of θ for the sample. If the sample does not undergo any other changes in its crystalline structure, the single peak is still present but shifted to account for the strain.

3.3.3. Oxidation dynamics

The tantalum samples were tested in an ambient pressure x-ray photoemission spectrometer (AP-XPS) at beamline 9.3.2 of the Advanced Light Source (ALS) at Lawrence Berkeley National Laboratories (LBNL). Details on the instrument are presented in the subsequent sections. This particular device is one of only two XPS in the world capable of working at high pressures up to 10 torr allowing the tantalum samples to be exposed to a controlled environment.

The end-station at beamline 9.3.2 is composed of three chambers: a load lock, sample preparation chamber, and testing chamber. The sample preparation chamber is equipped for Argon ion etching. The testing chamber is made specifically for high-pressure XPS analysis, which is discussed in detail in the subsequent section.

All testing was performed on the flat, polished side of the tantalum samples. The samples were ion etched in the preparation chamber for 2 minutes at 2keV to remove native and subsequent growth-controlled oxides prior to testing. The samples were then transferred to the testing chamber which is at ultra-high vacuum conditions at the time of transfer. XPS tests were performed at a photon energy of hυ=550eV. An initial survey scan is performed to identify the regions of interest; tantalum 4f edge, Fermi edge, and

carbon 1s edge. Focused scans at a resolution of .1eV/step where performed at the C1s and Ta4f edges to verify initial conditions and the removal of oxide from the surface.

XPS tests were performed *in-situ* during the oxidation processes to monitor reaction dynamics. Focused scans of .1eV/step resolution and lasting 45sec each where performed continuously at the Ta4f edge. Scans began prior to the release of oxygen to obtain a baseline initial state. Oxygen was then released into the testing chamber at a pressure of 0.1 torr. The reaction was scanned and allowed to continue until it was evident that the sample had achieved a stable state. At the end of the oxidation process, oxygen inflow was stopped and the chamber was allowed to reach ultra-high vacuum conditions. A focused scan of the Ta4f and C1s edges was repeated for verification of the final oxide states.

The sample was then returned to the preparation chamber where the surface was Ar etched. *In-situ* oxidation measurements were performed for each sample at four different temperatures, as shown in Table 4. The samples were heated by a ceramic heater placed below the sample. Temperature was monitored at the surface on the testing side of the sample.

Table 4. *In-situ* oxidation conditions tested

Sample	Temperature (K)	Oxygen Pressure (torr)
	300	
	400	
Ta (100)	500	
	600	
		0.1
	300	
	400	
Ta (100)- Compressed	500	
	600	

3.4. Characterization

Wear debris was collected by rinsing the samples with methanol into a glass vial. The solution was drop cast unto silicon (100) substrates approximately 12mm x 10mm in size. Deposition was continued until a visible coating developed on the substrate.

X-ray spectroscopy characterization was performed on the wear debris. X-ray adsorption spectroscopy (XAS) was performed at beamline 8.0 at the Advanced Light Source (ALS) in Lawrence Berkeley National Laboratory (LBNL) at Berkeley, California and at beamline 9.3.1 at ALS in LBNL. . Finally, X-ray photoemission spectroscopy (XPS) was performed at beamline 8.0 at the Stanford Synchrotron Radiation Lightsource (SSRL), part of the Stanford Linear Accelerator Center (SLAC) National Accelerator Laboratory at Stanford University, Menlo Park, California and at

beamline 9.3.2 at ALS in LBNL. A brief description of each method and purpose is presented in the following sections.

3.4.1. X-ray adsorption spectroscopy

3.4.1.1. Brief background

X-ray adsorption spectroscopy (XAS) is a method used to determine the electronic structure of matter. This technique is particularly sensitive to the local structure of the atoms and is often used for studying doping, ion implantation, gases, solutions, solids, and organo-metallic compounds [91]. This method is particularly useful for organic films due to its ability to probe core and unoccupied valence states[92].

XAS is typically performed at a synchrotron radiation source where the user can tune the exciting photons with a monochromator. The principle of XAS is that as the incident photon energy is swept from low energy to higher energy, it will begin to excite very specific electrons [93].During the beginning of the energy sweep, when the photon energy is below the binding energy of all electrons in the sample, the will be no effect on the sample, as seen in the first image in Figure 21. As the photon energy reaches the binding energy of a particular electron shell, an electron will be excited and forced to jump out of its shell. However, the kinetic energy of this electron remains too low and is absorbed in the valence or conduction bands. When the photon energy exceeds the electron binding energy, the electron is emitted into vacuum.
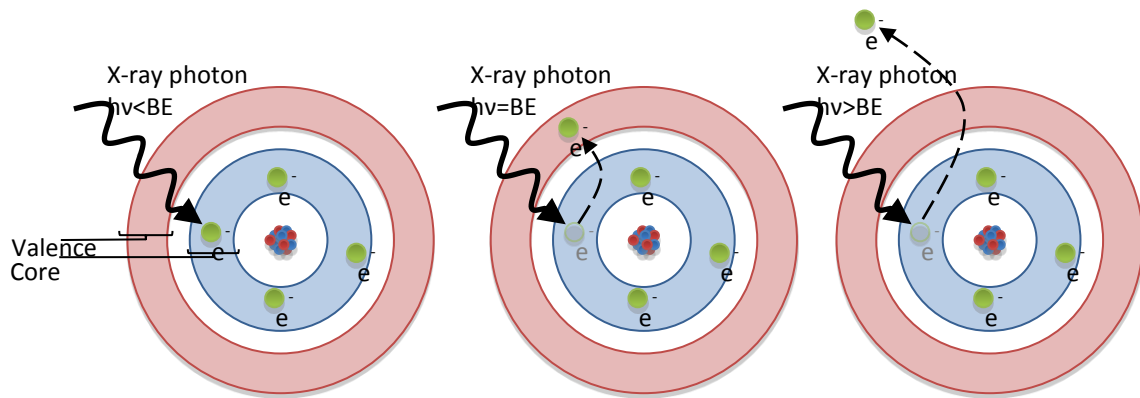
Figure 21. In XAS, photons emit specific electrons which escape at a
certain photon energy and with a characteristic kinetic energy for each
element

3.4.1.2. Data analysis

XAS methods measure the number of electrons emitted at a particular photon

incident energy. The data is plotted as an intensity (number of electrons detected) vs.

incident energy, as shown in Figure 22. Of particular importance is the rising edge which

is the edge at which a high density of electrons are achieving energies large enough to

escape the solid continuum.

Since the emitted electrons undergo collisions with other electrons and are

affected by surrounding atoms, the exit kinetic energy is affected by minute, yet

detectable amounts. This ability to be affected by the continuum allows for a specialized

local survey of the sample near the atoms.
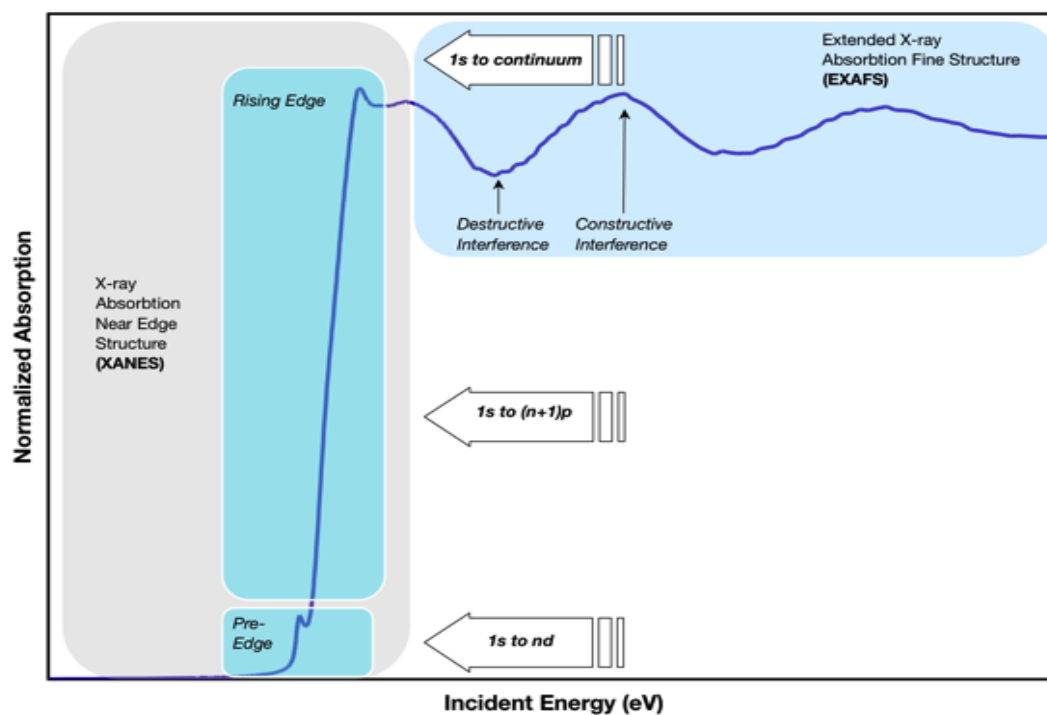
Figure 22. Different regions of X-ray adsorption study different regions
of the electron cloud and chemistry

3.4.2. X-ray photoemission spectroscopy

3.4.2.1. Background

X-ray photoemission spectroscopy (XPS) is a method used to determine the electron shells and chemical state of an atom[94].The data obtained allows the quantitative measurement of the electronic states of an element[95]. . Such measurements and changes to these measurements are correlated to the binding energy of the electrons, which are very particular to the element and shell they belong to.

In the XPS method, x-ray photons excite electrons causing them to get energized and shift from their ground state. If the photon energy, hv, is equal or below the binding

energy of a particular electron, the electron will simply shift to a higher energy subshell. Electrons that are excited into higher energy shells return to their ground state after the x-ray excitation is removed [96]. If hv is sufficiently above the binding energy, the electron will be emitted and lost into vacuum.

Emitted electrons will have an energy corresponding to the difference in the incident energy and the binding energy, as described in equation 2. The difference of the energies is translated into kinetic energy of the electron. Since each electron shell has different characteristic binding energies, electrons from each shell with have a characteristic kinetic energy as well.

$$Eb= hv+Ek \qquad\qquad (5)$$

As seen in Figure 23, the emitted electrons are captured by a hemispherical analyzer which bends the path of the electrons using strong electromagnets. Electrons with different kinetic energies will obtain different bend radii and hit an electron detector at the end of the bend. The detector monitors the location of the electron impact, and with knowledge of the magnetic field applied at the analyzer, measures the kinetic energy of the electron. The binding energy is calculated by equation 5.

Because XPS requires the ejection of an electron, essentially ionizing the atom, it is very sensitive to the chemical environment it finds itself in. Though elementally the same, carbon can have very different binding energies, ranging up to several electronvolts, depending on what other elements it is coordinated with. This makes XPS a very useful tool in determining the activity and reactions of materials. XPS is limited

to properly probe surface elements, between 5-40nm [7] depending on the materials

adsorption coefficient, crystallinity, and orientation amongst several other factors.
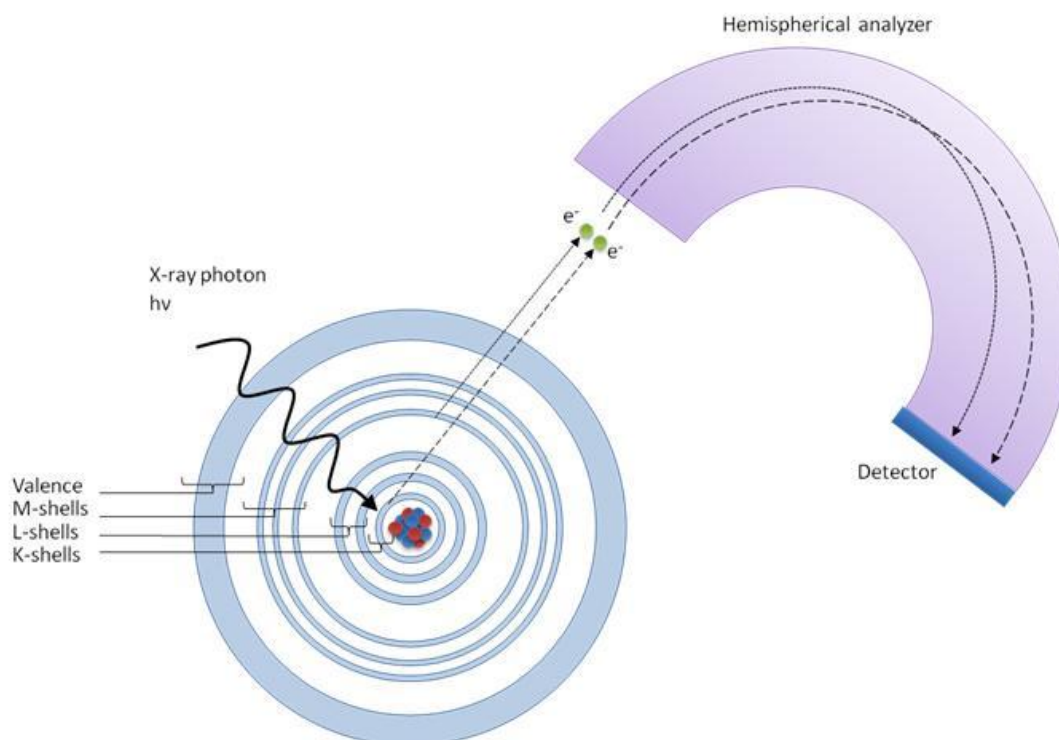
Figure 23. Principles of XPS. Photons with sufficiently high energy are
able to eject core electrons which have a special signature depending on
chemical and electron state of the atom

3.4.2.2.   Ambient pressure XPS

Typical XPS instruments require operation at ultrahigh vacuum, below 1×10^{-6}

torr. High vacuum is required in such experiments to increase the mean-free-path of

electrons emitted from the sample. At higher pressures, electrons would collide with gas molecules and scatter away from the analyzer. However, the ambient pressure x-ray photoemission spectrometer (AP-XPS) located at beamline 9.3.2 in ALS of LBNL employs a novel method to allow operation at pressures of up to 10 torr[97]. The chamber allows the gases in the testing chamber to evacuate through the same aperture as the electrons, ensuring that both molecules and electrons travel in as similar of a path as possible. Like cars in a freeway, if all particles are flowing in the same direction, the probability of collision is reduced and thus extending the mean-free path of the electrons. However, the high pressure gas exiting the testing chamber needs to be removed in such a way that it does not interfere with the electrons prior to reaching the analyzer. To do so, the AP-XPS uses a series of chambers, each at a lower pressure than the previous, until the electrons reach a chamber at near ultra-high vacuum. A simple schematic of the theory (left) and application (right) is demonstrated in Figure 24.
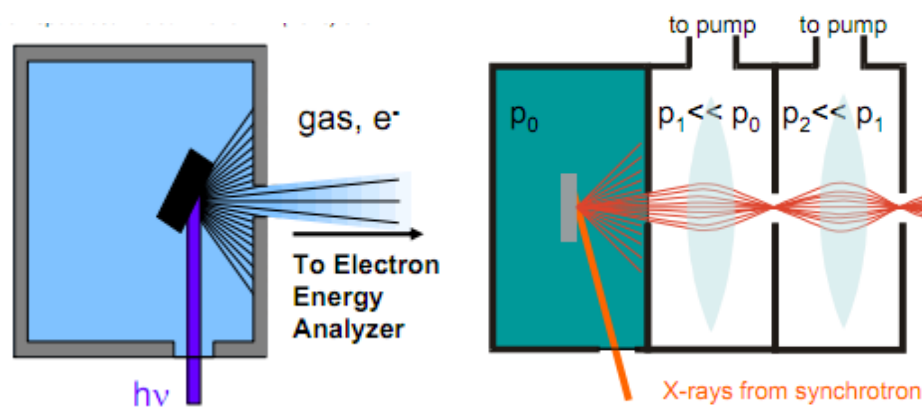
Figure 24. X-rays enter through a small window into a high pressure chamber where the sample is located. The gas flows through the same aperture as the electrons towards the detector, reducing the probability of collision between electron and gas molecule

3.4.2.3. Data analysis

Quantitative and qualitative information of the sample can be extracted from XPS spectra. Data obtained from an XPS is presented by plotting intensity vs. binding energy, as seen in Figure 25. The plot shown is an artificial signal representative of a full survey scan of a non-existent sample. Each major identifiable peak corresponds to a particular electron orbital. Typically, but not exclusively, the larger peaks correspond to the most inner electron orbital. The further the orbital is from the nucleus, the probability of an electron being ejected reduces exponentially due to lower electron density at each subsequent orbit.
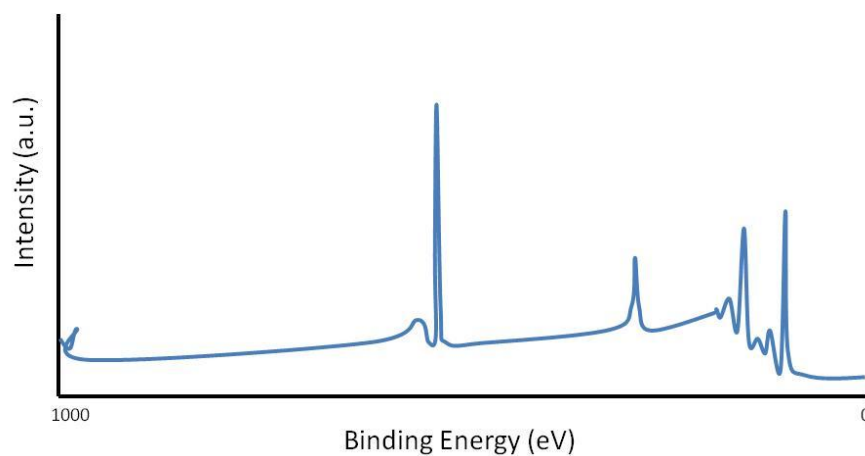
Figure 25. An artificial XPS spectra is typically shown in decreasing
binding energy. The highest intensity peaks are of the closest electron
shells, while less peaks with lower binding energy typically correspond
to shells further from the nucleus

Though the highest and cleanest signal would be obtained from the inner-most orbit, for many elements, these orbits do not have much interaction with their

environment. To perform studies on the electronic state of an atom, the outer-most complete shells are more significant. These shells are more susceptible to minute changes in their environment.

A closer look at one of the peaks obtained in the artificial signal above shows that the peak is composed of smaller peaks, as seen in Figure 26. These peaks convolute into the larger raw signal. With proper knowledge of the sample, one can deconvolute the signal to obtain the position and intensity of each peak. For basic analysis, this can give sufficient information as to the surface composition and bonding mechanisms. However, with a high resolution scan, one can distinguish small ($<1eV$) shifts of the peaks. These shifts can be due to chemical or mechanical changes in the bonds resulting from changes and reactions to the chemical environment.
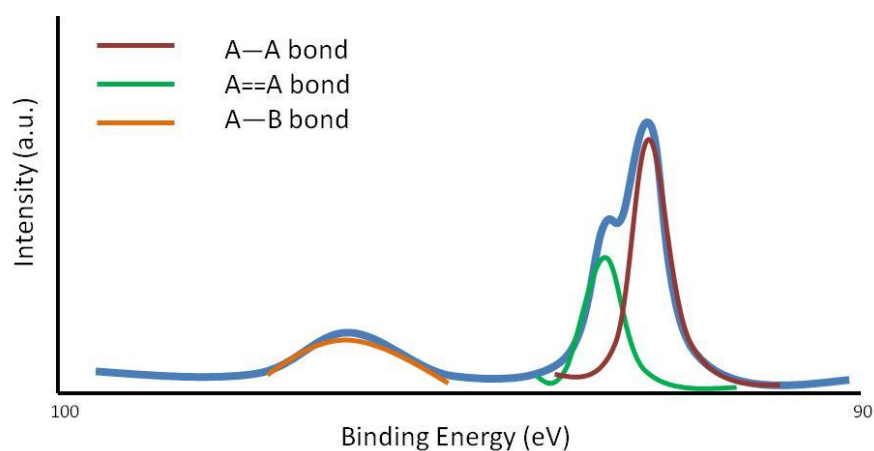
Figure 26. Deconvolution of the raw signal shows the position and ratio of bond-specific binding energies. Changes in the chemical environment would appear as shifts of the positions of any one or all of the smaller peaks

In this research, spectra deconvolution was performed using CasaXPS software. A Shirley background removal was implemented and the curves were modeled as a mixed Gaussian and Lorentzian profiles. All spectra are referenced to the Fermi edge, which is the point at which no electron is emitted.

CHAPTER IV

MECHANICALLY ACTIVATED WAX MOLECULES

In tribological applications, a lubricant is used to reduce friction and wear of two mating interfaces in motion. In this chapter, we inspect a nature-produced wax for activation due to a tribological wear procedure. This chapter will firstly investigate the tribological properties of the biologically generated wax followed by the effects on the substrate sample. It will then transition into spectroscopy analysis of the wax and debris created during the tribological testing and the significance of such results.

4.1. Substrate analysis

4.1.1. Tribological testing

As mentioned in the methods chapter, a biological wax was obtained from *Periplaneta americana*, commonly named as the American cockroach. As described in the introduction, the wax was composed of many different length paraffins, alcohols, and esters. A model of such composition is shown in Figure 27, created by Material Studios software. Each differently colored branch represents a different ester, paraffin, or other component of the wax. The composition of the biological wax is of great interest due to the high variability in molecular length of each component. Differing lengths can create different responses to shear, much like polymer chains during tensile deformation[98-99].

Friction tests were performed as described in the methods chapter with a linear reciprocating motion tribometer made by CSM, Inc. One testing substrate was clean

stainless steel 316 and the other was the same material but with a wax coating applied as previously described. The average of five tests for both substrates is shown in Figure 28.
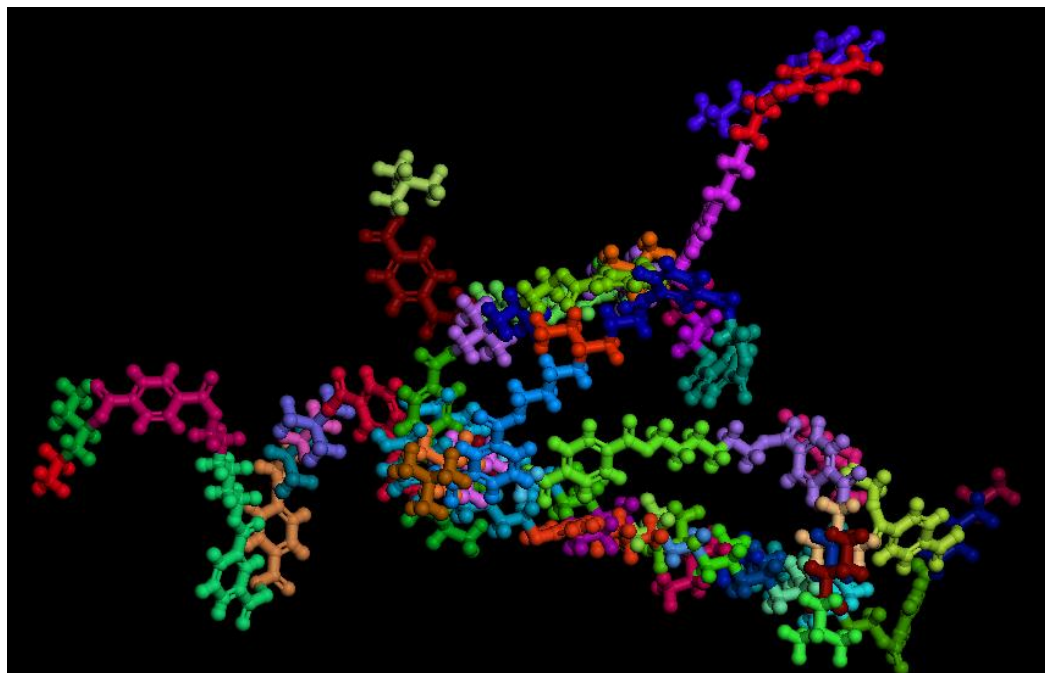
Figure 27. Modeled biological wax composed of multiple length chains
of paraffin, esters, and alcohols

It can be seen that the friction coefficient is reduced significantly with the addition of the bio-wax. In the initial stages of the tribology tests, below one minute, the dry sample exhibited a sudden increase in friction, which the lubricated sample did not. The lubricated sample maintained a low friction with little variance throughout the duration of the experiment. The dry sample exhibited a large amount of fluctuation after the initial rise in friction. The initial increase is attributed to a "wearing in" phase[100-104].

After this initial phase, the dry sample changed wear mechanisms repeatedly from smoothing due to abrasive wear[104-107]to stiction due to increased surface contact[108-110].
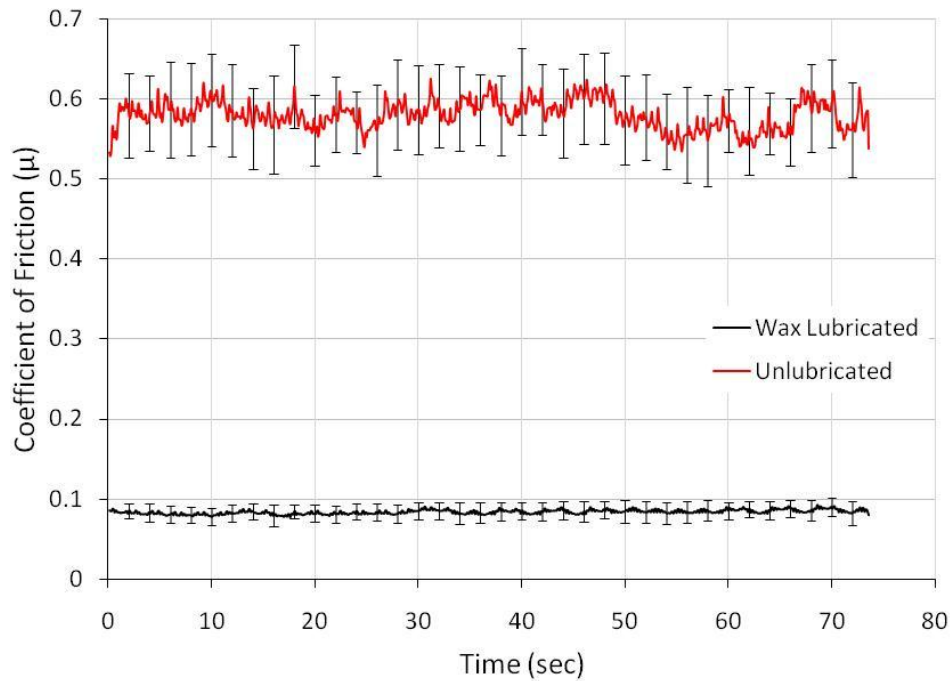
Figure 28. Friction coefficient of stainless steel substrates with and without a wax coating for lubricant

4.1.2. Surface analysis

The wear track created by the reciprocating motion of the pin against the stainless steel substrate was analyzed by nanoindentation techniques. A Berkovich diamond tip was used to produce an indent into the substrate to obtain a depth profile of modulus of elasticity and hardness. Both samples were cleaned to ensure no wax remained on the surface.

The modulus of elasticity for the unlubricated sample showed a typical trend of nanoindentation on a wear track. As shown in Figure 29, the value of the modulus increased quickly within the first hundred nanometers in depth before slowly degrading to its bulk value. This is likely caused by a type of hardening due to straining of the surface. For the sample with roach wax lubrication, this increase in modulus near the surface is absent. It is pertinent to claim that the wax film created a boundary lubrication layer sufficient to avoid placing as much pressure at any given point and reducing the effects of hardening.
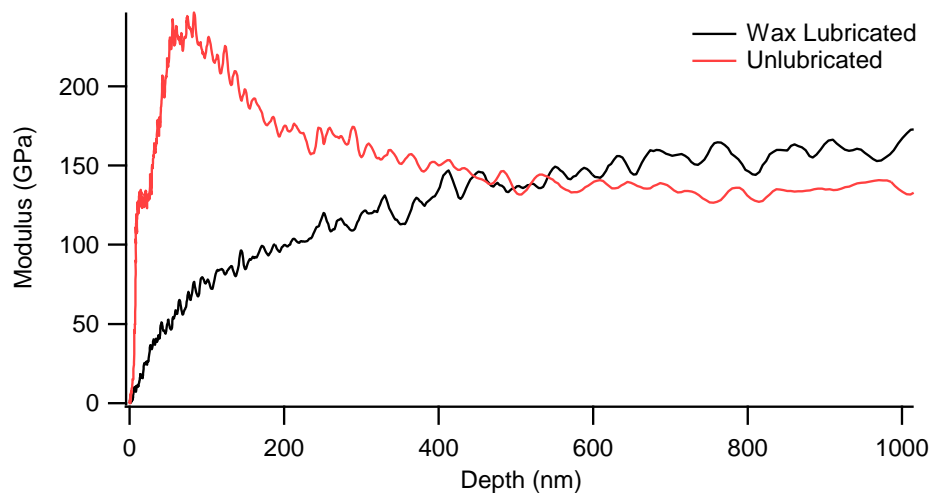
Figure 29. Modulus of elasticity derived from nanoindentation results
show different effect of case hardening due to contact interference

The same is seen in the hardness depth profile shown in Figure 30. The unlubricated sample shows a quick increase within the first 100 nm before a slow decent

into the bulk material value. Similarly as with modulus, the lubricated specimen shows

no sign of this case hardening.
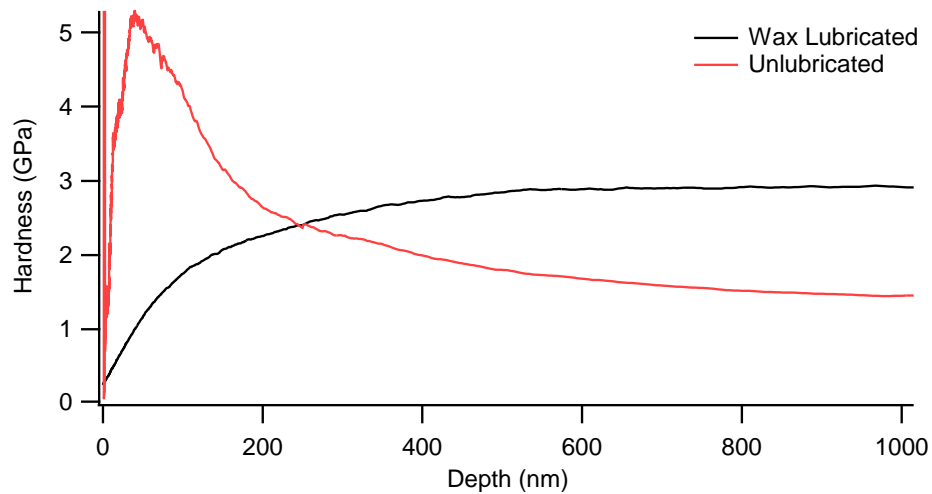
Figure 30. Hardness derived from nanoindentation results show
different effect of case hardening due to contact interference

4.2.   Spectroscopic analysis

4.2.1. XPS analysis

X-ray photoemission spectroscopy (XPS) studies were performed at beamline 8.0

of the Stanford Synchrotron Radiation Light source (SSRL) at Stanford University.

Studies were performed to identify the activation of the roach bio wax upon

reciprocating friction stimulation. Energy is introduced into the bio wax via heat and

mechanical straining while wear debris is simultaneously created.

The debris for the unlubricated and lubricated samples was collected as described in the Chapter III and deposited onto a Si (100) wafer for XPS studies. Scans were performed in survey mode, sweeping over a large energy range to fit the Fe-2s, C-1s, and O-1s peaks in the same measurement. The spectrum for each sample is shown in Figure 31.
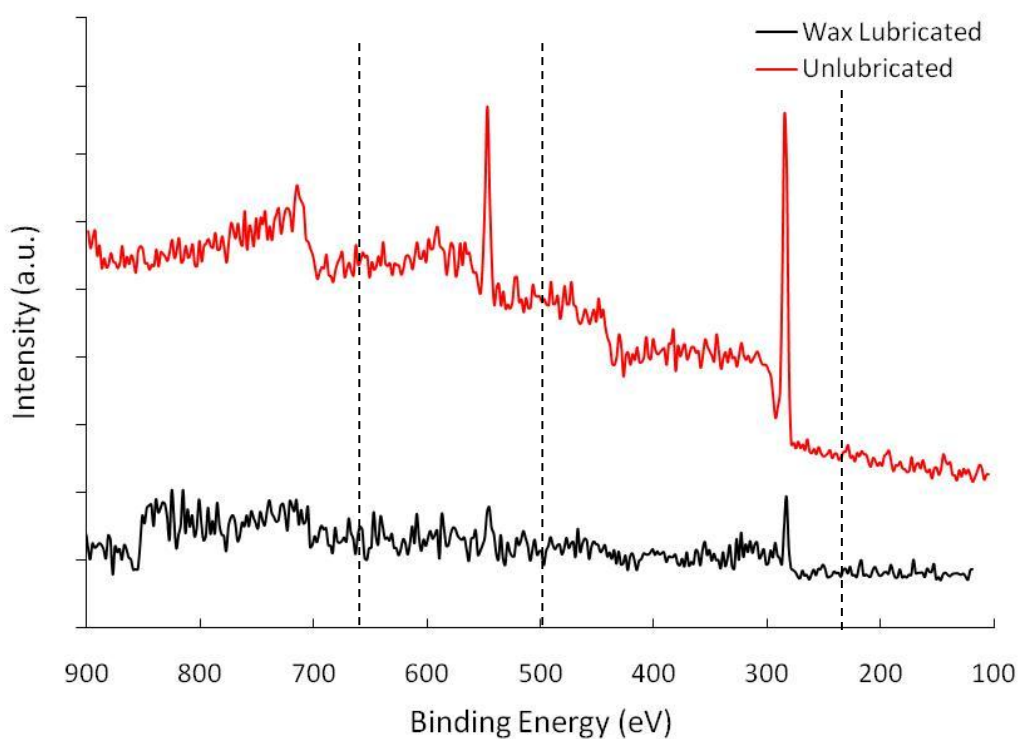
Figure 31. XPS data for friction induced wear of stainless steel
substrate with and without a wax lubricant coating

Spectroscopical analysis of the lubricated sample has a much more subdued signal for the debris with roach wax due to the electrical insulation properties of the

roach wax. The penetration depth of the XPS is about 10-50 nms. Encapsulated by roach wax, the metallic peaks were difficult to obtain. Deconvolution of the data was performed using the software XPSpeak. Relative intensity studies of the peak were unsuccessful due to the amount of noise added by the roach wax. Peak positions of the three elements and orbitals mentioned previously were calculated from the spectra obtained. These values are shown in Table 5.

Since the C-1s peak is commonly used as a point of reference due to its thermal and chemical stability, the lubricated and unlubricated wear debris spectra were adjusted to match the reference peak. It can be seen that with such adjustment, the O-1s peak exhibited a slight shift of 0.9eV to a lower binding energy. Shifts in the peak position of XPS spectra can either be due to chemical state of the element or to thermal variations in the material. Since these experiments were performed at the same temperature, this shift is suggestive that the samples have undergone some form of oxidation[111-112].

Typically, oxidation of a metal results in a higher binding energy due to a more stable and less reactive oxide state. Contrary to this, Table 5 shows that the Fe-2s peak shifts to a lower binding energy, invalidating this condition.

Table 5. Peak positions of various elements identified in the XPS
spectra compared to published reference samples

	Binding Energies (eV)		
	C-1s	O-1s	Fe-2s
Reference	284.2	543.1	719.9
Unlibricated	284.2	546.2	716.2
Lubricated	284.2	546.2	714.2

Iron typically forms compounds in which it attains oxidation states of +2 and +3. These states would cause the binding energy to shift to a higher value than the reference sample. However, in very rare circumstances, iron is able to produce compounds with an oxidation state of -1 and -2 which would agree with the reduced binding energy seen here. One such instance of a compound with a -2 valence is known as ferrocene[113]. Ferrocene is an unstable compound in a relatively modern field called organometallic chemistry[114] and no x-ray spectroscopy studies have been found at the time of this writing. Ferrocene is composed of an iron atom sandwiched between two aromatic carbon rings, as shown in Figure 32. Subimage a) shows the 3D structure of ferrocene, as modeled by Materials Studio, and b) shows the chemical representation as previously identified by other researchers [114-116].
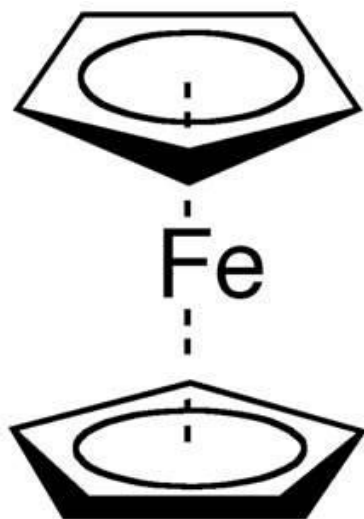
Figure 32. Ferrocene composed of an iron atom sandwiched between
two carbon aromatic rings

4.2.2. XAS analysis

While XPS is good in determining the chemical bonding of different elements, it can be hampered by non-conductive, organic coatings. XPS will allow for a chemical state of an element, but XAS can give information on the electronic structure of that element. In other words, XAS spectra can give an insight as to the interaction of the wax and the wear debris.

X-ray adsorption spectroscopy was performed on the same samples as used for XPS analysis. A reference iron sample was used for calibration and monitoring peak shifts of the iron debris. The spectrum for the reference sample is shown in Figure 33. The two major peaks shown correspond to the iron 2-p orbital orbitals. The larger of the peaks corresponds specifically to the $2p_{3/2}$ sub-orbital and corresponds to an energy of 706.8eV. The smaller peak corresponds to the $2p_{1/2}$ sub-orbital and corresponds to an energy of 719.9eV. A curve-fit analysis was used to identify the peak position for the

sample with no lubrication and with roach wax as a lubricant, shown in Figures 34 and

35, respectively. These values are summarized in Table 6. The curve-fit method used

was a built-in function in the IgorPro software and based on a Voigt curve shape.
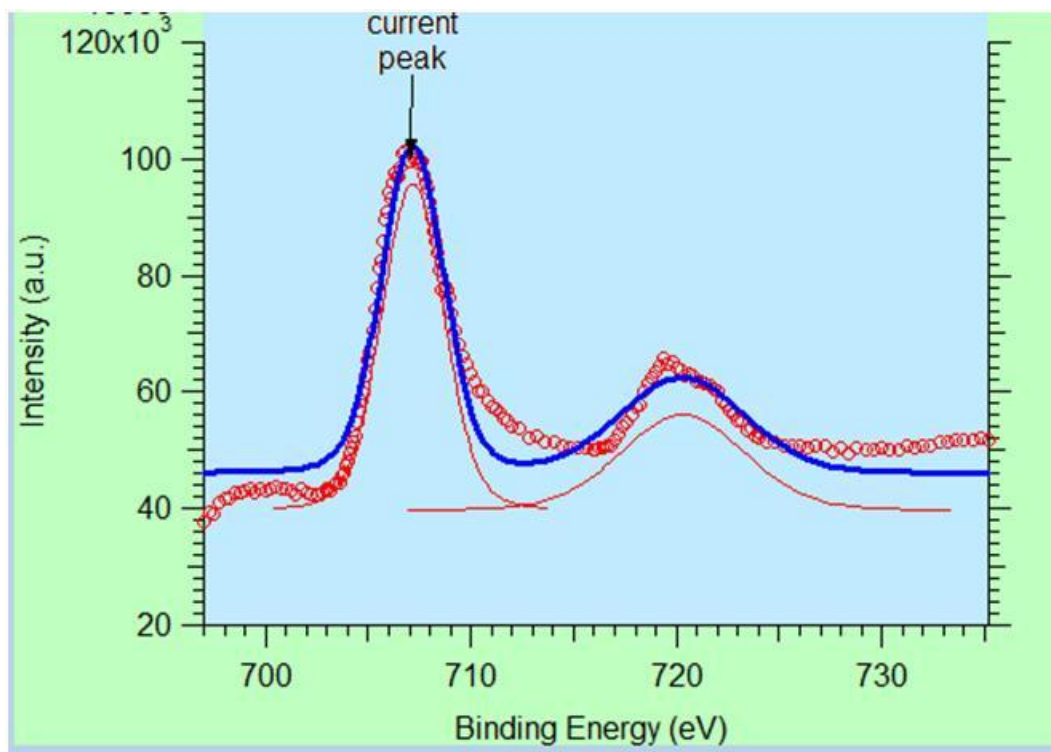
Figure 33. XAS spectrum of iron bulk sample identifies 2 major peaks
of the 2p orbitals
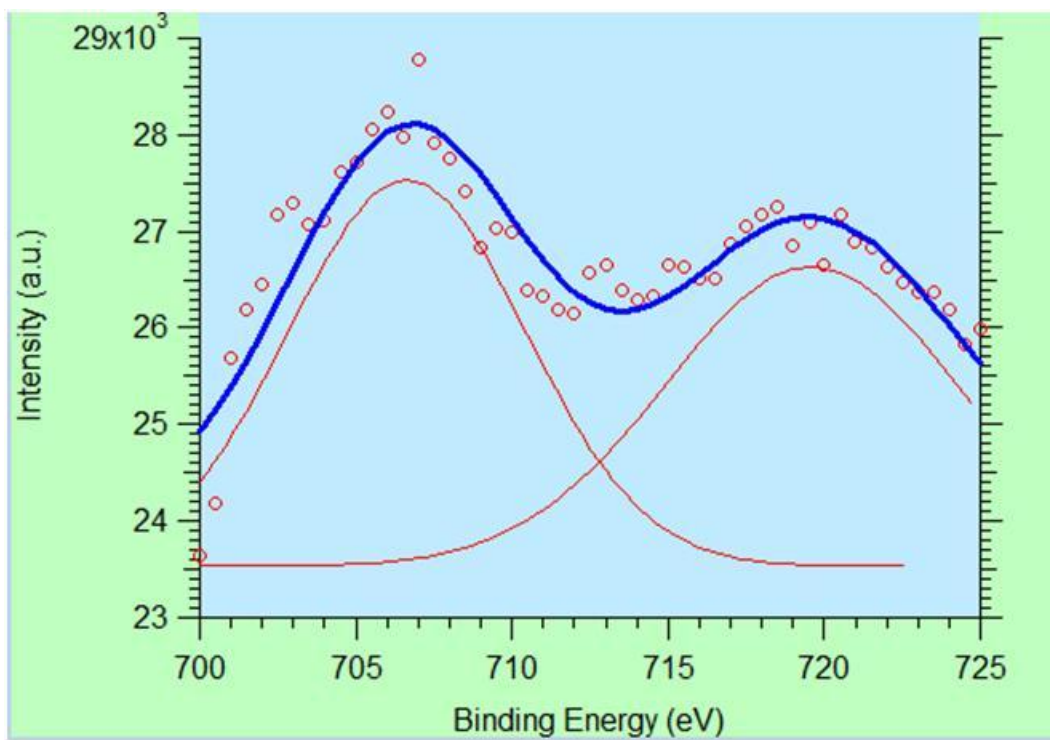
Figure 34. XAS spectrum of unlubricated wear debris sample
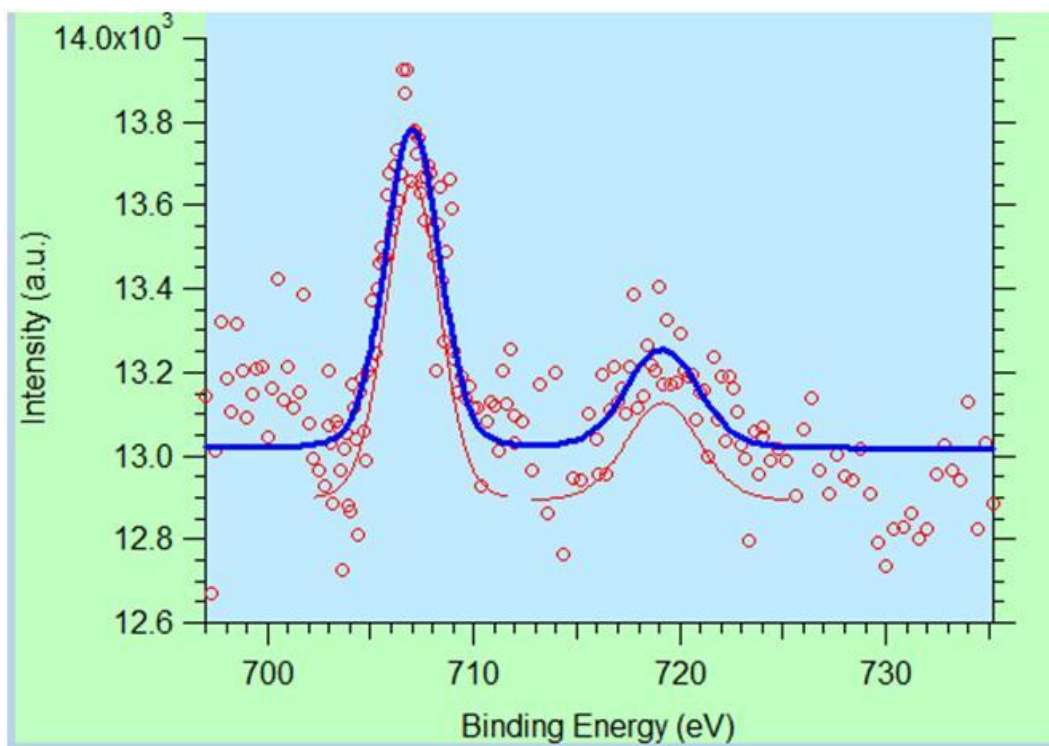
Figure 35. XAS spectrum of the wax lubricated wear debris samples

Table 6. Peak position of iron 2p orbital energies as identified by
IgorPro

	Orbital Energies (eV)	
	L $2p_{1/2}$	L $2p_{3/2}$
Reference	720.22	707.04
Unlibricated	719.12	707.07
Lubricated	719.14	706.00

There are many possible explanations for the shift in the energy of the $2p_{3/2}$ peak.

Peak shifts are often seen for transformations from intrinsic metals to oxides [117-119].

However, these shifts typically result in increased energies and only by a range of less than 0.5eV. It is believed that a shift to a lower energy would be a factor simply on structural effects, particularly as samples decrease in size from bulk [120-122]. Even more convincing, though, is the idea that a shift to a lower energy is due to a lower mean valence of metal ions [123-124], which is consistent with the previous XPS results. Previous studies have shown that a decrease of 1eV per ionization degree reduction[125-127].

4.3.   Summary

This chapter investigated mechanisms of a biologically made lubricant. Comparative study was conducted on two samples, a stainless steel substrate with a clean surface, and another coated with the lubricant. A biologically produced wax was applied to one substrate as a lubricant for tribological applications. Studies on the effects of the biological lubricant were performed on both the substrates and debris. A stainless steel ball exerted a normal force against the substrate producing a wear track.

We have seen in this chapter how the lubricant was able to prevent significant impact on the subsurface of the substrate. Hardness and modulus depth profiles show that an unlubricated sample experienced a level of hardening, as is common in plastically deformed metallic surfaces. However, the lubricated sample showed no signs of this hardening as the values for hardness and modulus increased proportionally with depth.

The debris of the samples was collected and inspected using x-ray spectroscopy methods. XPS data identifies the principal elements in the samples, carbon, oxygen, and

iron. Of these elements, iron exhibits a very large shift to lower binding energy. In the field of organometallics, a stable structure of ferrocene is described which is likely to be the structure corresponding to such a large lower shift.

XAS studies of the debris show a shift in the outermost covalent shell of the iron atom. The shift is to a lower energy suggesting that it is not due to oxidation of the atom. This shift is believed to be due to a reduction in ionization degree which corresponds to a 1eV shift to lower energy.

CHAPTER V

STRAIN-AFFECTED ACTIVATION

In this chapter, we present a method of evaluating the activation energy through a process of oxidation for single crystal tantalum specimens. We developed a special technique allowing us to apply and measure a strain on the crystal lattices and investigate how this added stress alters activation energy. We proceed from empirical data and develop a model to account for stress when calculating the theoretical activation energy.

5.1. Crystal characterization

5.1.1. Reference samples

The study of how strain can activate, or alter chemical reactions of tantalum, comparative studies had to be performed on reference and strained samples. Two sets of samples are used in this research. Each set, as described previously, will contain one sample of each major crystallographic orientation, (100), (110), and (111). The first set contained one sample of each orientation and was prepared only by polishing the tested surface. The second set required a known amount of strain to be introduced into the crystal lattice. Distinction between each sample will be made by referring to the samples by their orientation and either reference or strained.

Initial crystal characterization of the samples was performed on all the samples. X-ray diffraction (XRD) analysis was performed to verify the crystal structure and provide a baseline for measuring strain in the lattice.

An XRD spectrum for the Ta (100) sample is shown in Figure 36. The plot displays a single, narrow peak at 55.6° with negligible background noise. Using Bragg's law shown in equation 1 in Chapter III, we can calculate this angle to correspond to a plane spacing of 3.312nm which is consistent with the planar spacing of a (100) tantalum sample. The calculated values for the plane separation for each sample are given in Table 7. These values are consistent with literature [128]. Figure 37 and Figure 38 show the spectra for a tantalum in the (110) and (111) orientation, respectively. Similarly, both of these spectra display a single, narrow peak as would be expected for single element, single crystal samples. The structure and plane separation for each orientation are confirmed in Materials Studio and shown in Figure 39.

Since XRD functions by wave interference, as described in Chapter II, this denotes a single two-theta angle at which the reflected waves produce constructive interference. This is indicative of two important facts of the sample: the sample is composed of a single element and of a single crystal orientation.

The location of the peak is also characteristic of the sample's composition and orientation. The 2θ value of the peak can be used to calculate the plane spacing, d, using Bragg's shown in equation 1 of the methods chapter.
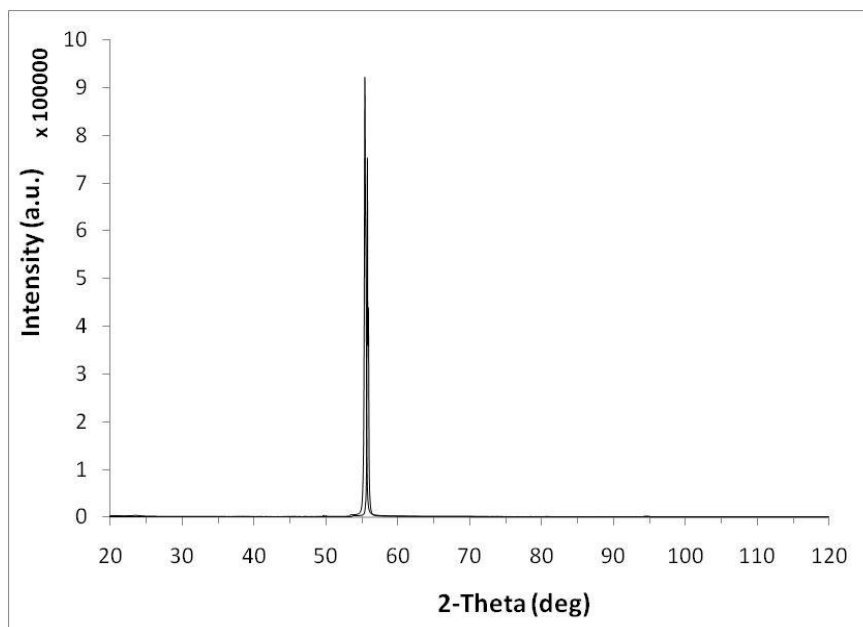
Figure 36. Ta (100) single crystal XRD spectra
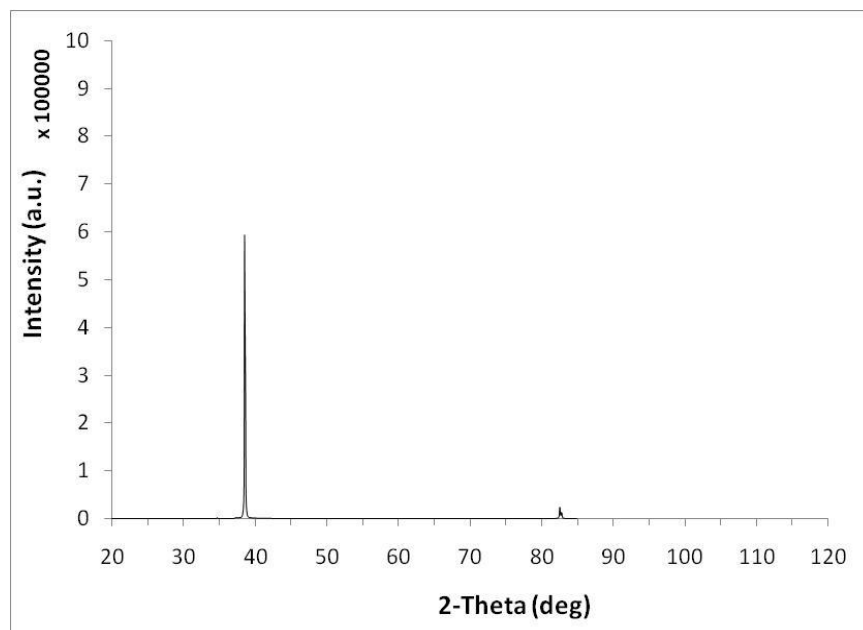
Figure 37. Ta (110) single crystal XRD spectra
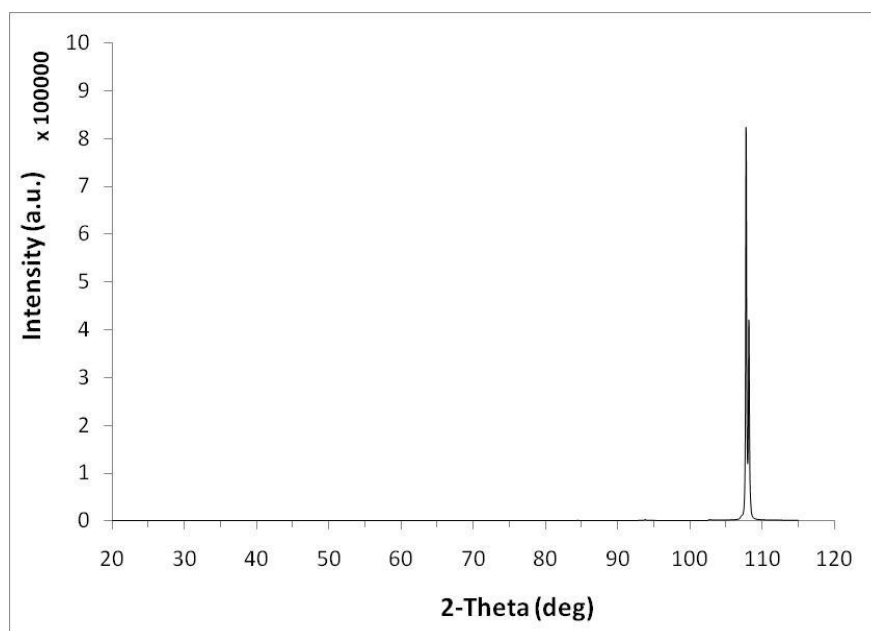
Figure 38. Ta (111) single crystal spectra

Table 7. Crystal plane separation, d, as measured using Bragg's law
and the XRD spectra for each sample

Crystal Orientation	$2\text{-}\theta_0$	Plane spacing (Å)
100	55.663	3.312
110	38.539	4.680
111	107.741	1.914
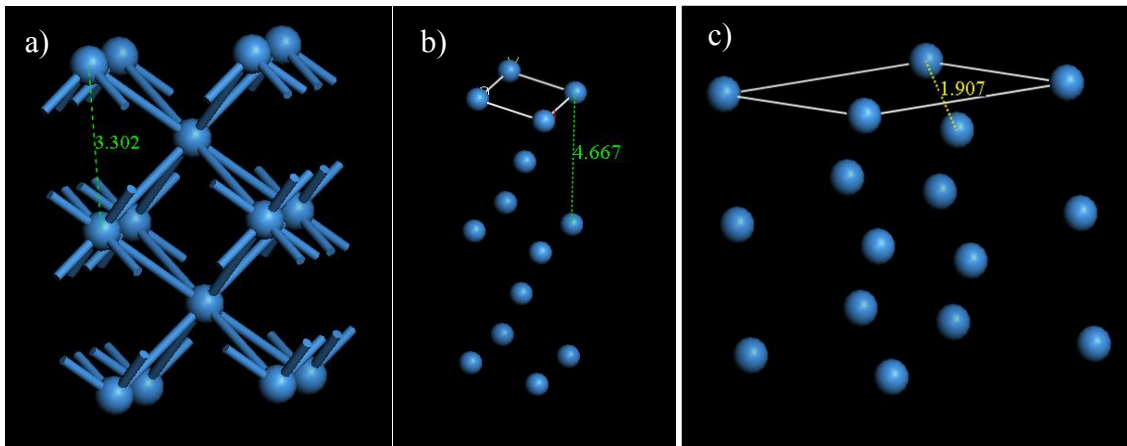
Figure 39. Structure and plane separation as modeled by Materials
Studio Software for a) Ta(100), b) Ta(110), and c) Ta(111)

5.1.2. Strained samples

5.1.2.1. Crystal structures

The second set of samples was strained as described in the methods section using an Instron compression/tensile tester. Special attention was placed on the samples during compression to avoid cracking or other destructive damage.

The three samples in the strained set were reinvestigated with XRD analysis. Figure 40 shows a close up of the region of interest of the Ta (100) sample. The black plot is of the reference sample and the red is for the strained sample. The strained sample still has a distinctive single, narrow peak with negligible background indicating a resilient single crystal structure. However, the peak is shifted from the reference 2-θ value by approximately 0.214°.
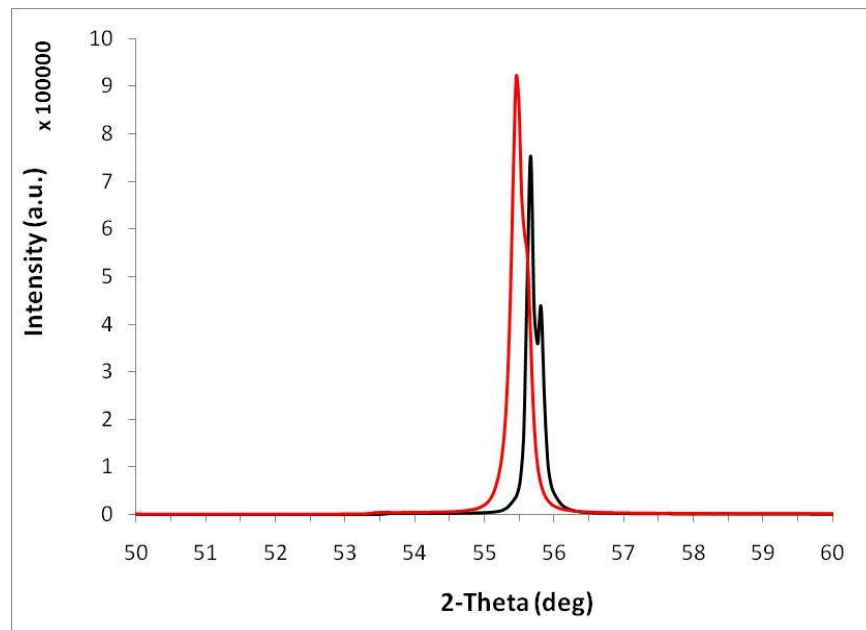
Figure 40. XRD spectra of tantalum (100) reference (black) and
strained samples (red). A peak shift is indicative of an alteration in the
crystal structure of the sample

The same can be seen for the strained Ta (110) in Figure 41 and the strained Ta

(111) in Figure 42. The extent to which the peak shifts varies due to the mobility of

atoms depending on the atomic planar density. Using Bragg's law again, the planar

separation is recalculated for the shifted peak. A summary of the plane spacing and

strain of the samples is shown in Table 8. All samples experienced approximately 0.3%

strain, calculated as the percent difference from the original plane spacing.

Table 8. Bragg's law is used to calculate planar separation as a function
of the shifted 2-θ value after compressing with Instron tester.

Crystal Orientation (strained samples)	2-θ_s	Plane spacing (Å)	Strain (%)
100	55.449	3.300	0.355
110	38.443	4.668	0.239
111	107.186	1.907	0.356
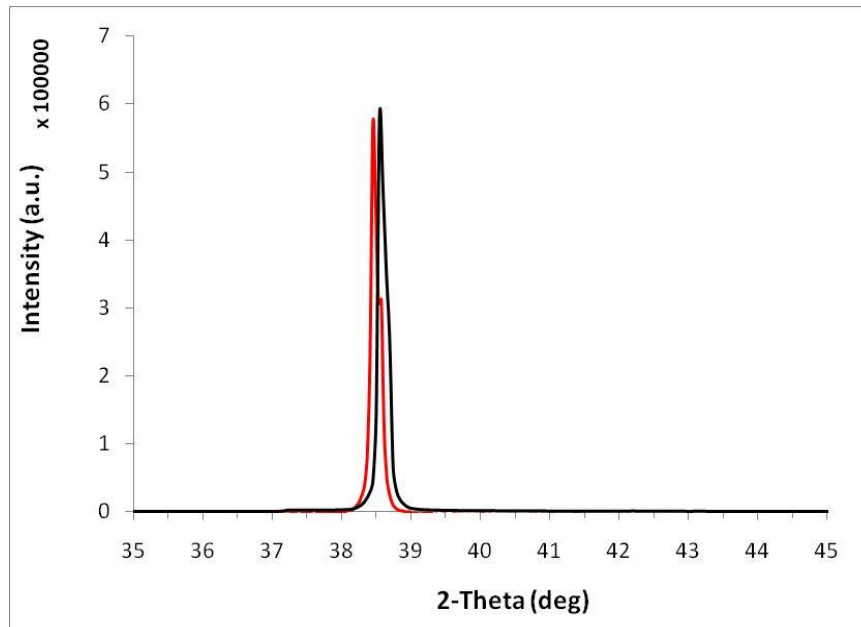
Figure 41. XRD spectra of tantalum (110) reference (black) and
strained samples (red)
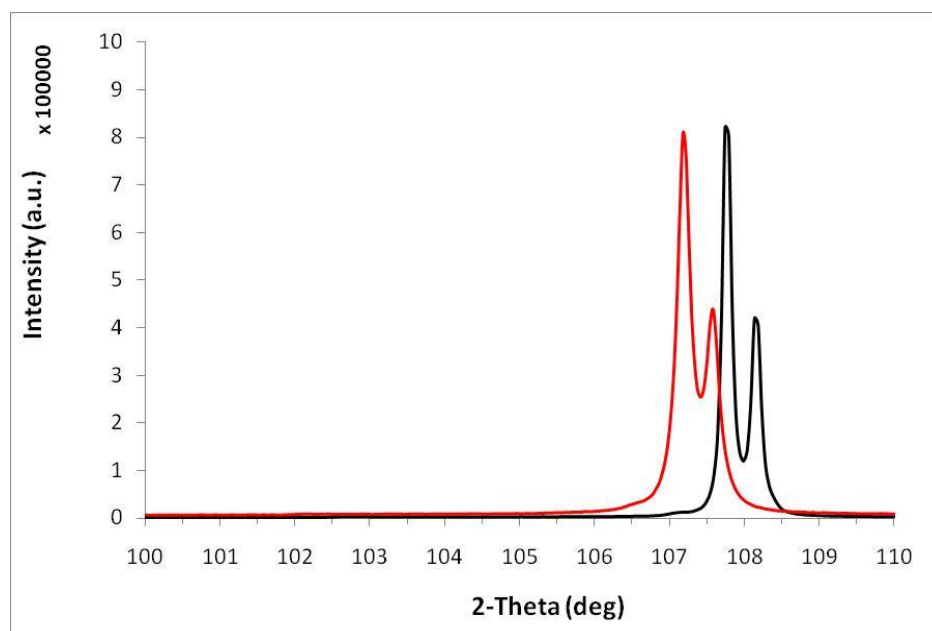
Figure 42. XRD spectra of tantalum (111) reference (black) and
strained samples (red)

During the compression process, the plastic deformation occurred within the bulk
of the sample and eluded the surface at the central region of the sample. This region is
the place of interest for all future examinations.

While XRD is a good tool for measuring crystal structure and orientation, it is
not sensitive to twinning[129]. Surface boundaries on can function as early activation sites
for chemical reactions due to their higher energy. Topographic profiles and phase
characterization surveys were performed to evaluate the development of such
boundaries. An atomic force microscope (AFM, Pacific Nanotechnology, Inc) was used
to survey the surface of the samples. Phase images obtained from the AFM surveys,
shown in Figure 43, show virtually no changes to the surface structure of the samples

before and after inducing strain. The AFM surveys would be sensitive to any changes in the surface, such as phases, boundaries, and even finish. As can be seen from the images, the region of interest of the samples was unaffected by the deformation of the bulk.
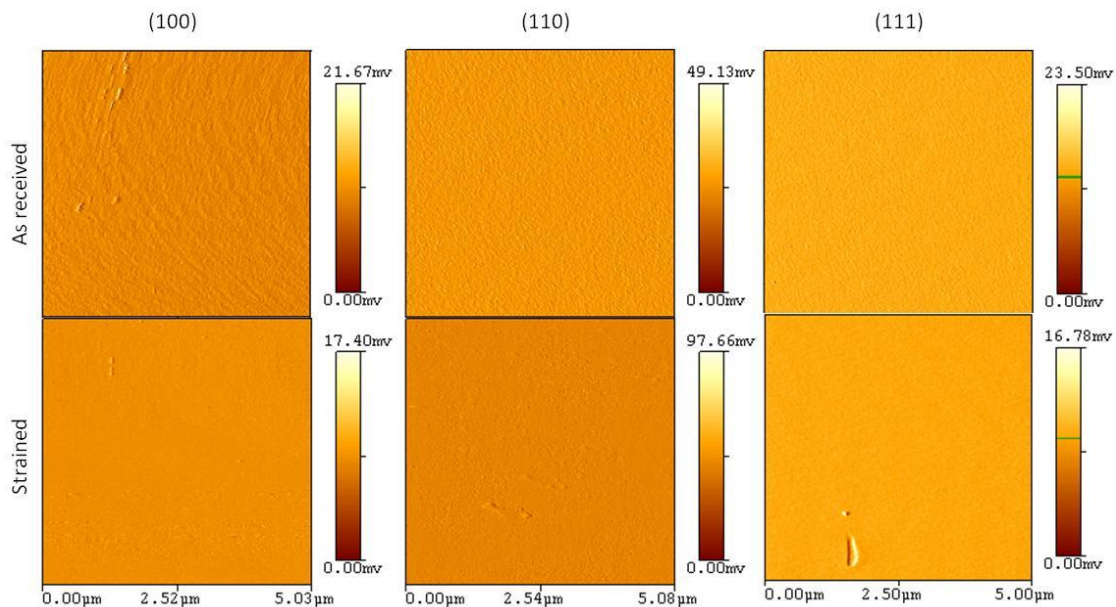
Figure 43. Phase images obtained from AFM surface surveys. There are no distinguishable changes in the surface of the samples before and after inducing strain

5.1.2.2. Lattice stress evaluation

Methods of calculating in-plane residual stress via XRD methods have been previously discussed in detail [88-90,130] and will only be covered in limited detail here. The strain developed by compressing the sample remained in the crystal lattices after deformation. This is evident from the XRD analysis previously shown. The resultant strain produces a residual stress in the crystalline.

Since the atomic packing factor changes for each crystal plane, differences in the material properties would be expected[131]. Poisson's ratio and the modulus of elasticity need to be defined in terms of each crystal orientation. To calculate these values for each orientation, we must begin from fundamental values derived from a single cubic crystal of tantalum[132]. In particular, the values of interest are the stiffness and compliance matrices, C_{ij} and S_{ij}, respectively[133]. The compliance matrix, [S], for tantalum is shown in Table 9, obtained from previously published data[134-136].

Table 9. Compliance matrix tensor value for tantalum

S_{11}	0.007021	GPa^{-1}
S_{12}	-0.002642	GPa^{-1}
S_{44}	0.012220	GPa^{-1}

Modulus of elasticity for each plane orientation has to be calculated by means of equation 6[87] . The subscripts *h, k,* and *l* are references to the Miller index coordinates. The values calculated for modulus of elasticity for each plane orientation are summarized in . The table also provides the common modulus of elasticity for polycrystalline tantalum.

$$\frac{1}{E_{hkl}} = S_{11} - 2(S_{11} - S_{12} - \frac{1}{2}S_{44})\frac{h^2k^2+h^2l^2+l^2k^2}{h^2+k^2+l^2} \qquad (6)$$

Table 10. Plane-specific modulus of elasticity of tantalum for each
principal plane

Plane	Elastic Modulus (GPa)
100	142.430
110	190.676
111	214.946
(bulk poly-crystal)	186

Similarly, Poisson's ratio for each plane has to be calculated. The values use the

same compliance matrix values as used previously. The method used for calculating the

in-plane Poisson's ratio is expressed in equation 7. The values obtained are summarized

in

Table 11.

$$
v_{hkl} = \frac{\left(S_{11}-S_{12}-\frac{1}{2}S_{44}\right)\frac{h^2k^2+h^2l^2+l^2k^2}{h^2+k^2+l^2}+S_{12}}{2\left(S_{11}-S_{12}-\frac{1}{2}S_{44}\right)\frac{h^2k^2+h^2l^2+l^2k^2}{h^2+k^2+l^2}-S_{11}} \tag{7}
$$

Table 11. Plane-specific Poisson's ratio of tantalum for each principal plane

Plane	Poisson Ratio
100	0.376
110	0.532
111	0.307
(bulk polycrystal)	0.340

Using Hooke's law, the strain parallel to the surface can be calculated using the modulus of elasticity and Poisson's ratio for each specific plane orientation. The values of the normal and surface strain is shown in Table 12.

Table 12. Normal and surface strain calculated after XRD analysis of
the compressed samples

Crystal Orientation	Normal Strain (%)	Surface Strain %
100	0.3552	0.1336
110	0.2395	0.1275
111	0.3561	0.1094

The lattice strain normal to the surface, ε_{hkl}, presented in Table 8 is now used to calculate the residual stresses present in the crystalline structures. Using equation 8 in a re-iterative process, stresses normal to the surface and parallel to the surface can be calculated.

$$E_{hkl} = \frac{1+v_{hkl}}{E_{hkl}}\left(\sigma_{norm} - \sigma_{surf}\right) + \frac{1}{E_{hkl}}\left(\sigma_{norm} - 2v\sigma_{surf}\right) \qquad (8)$$

Values for the stresses calculated from the above equation are shown in table 13 for each of the three samples. Note that the surface-parallel stress is negative, indicating a compressed condition on the surface of the sample.

Table 13. Normal stresses perpendicular to the surface and surface
stresses parallel to the sample surface are calculated for each sample

Sample Orientation	Normal Stress (Gpa)	Surface stress (Gpa)
100	0.506	-0.190
110	0.457	-0.243
111	0.765	-0.235

During uniaxial compression, the sample endured a complex deformation. Upon loading past the yield point, deformation began at the central volume of the sample causing a barrel-like deformation. This barrel deformation is caused by the contact interaction of the sample surfaces and the anvil presses. The result is a greater radial yield at the midsection than at the surface. Upon unloading, the midsection would have larger elastic recovery than the surface. The difference of recovery at the surface and center results in a compressive state on the surface.

5.2. XPS spectroscopical analysis

Continuous XPS measurements were compiled to provide a temporal evolution of the oxide formation. The temporal evolution of the Ta4f spectrum of the as-received Ta (100) sample at 600K is shown in Figure 44. Beginning from the top of the graph and progressing in time towards the bottom, there is a very evident transition in the spectra during the oxidation process. As can be seen, the spectra transition from two peaks near 22eV to two different peaks near 26eV. Additionally, each of the four peaks that appear

in the spectra appears to shift to a higher binding energy position as the oxide process develops. The shift is greater at 600K than at 300K. This shift could be due to a changing of composition ratios of suboxides Prior research has shown this shift to be indicative of impure oxide growth [111-112].

The spectrum, as mentioned previously, is the addition of background and multiple states and must undergo a deconvolution process to properly analyze the sample. This is presented in the following sections.
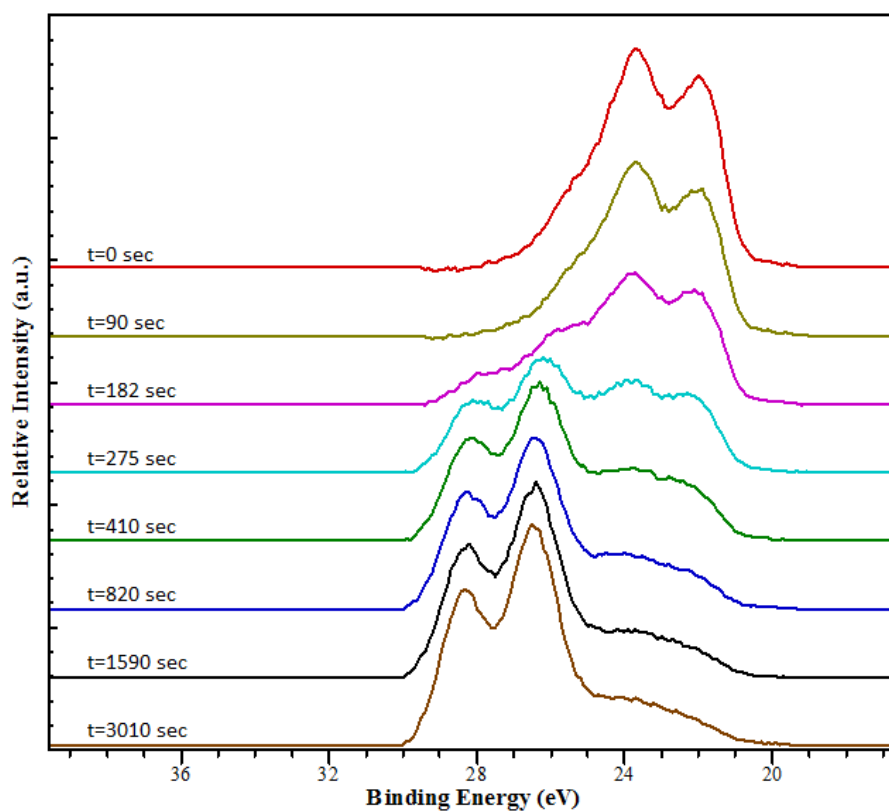
Figure 44. *In-situ* XPS spectra of temporal evolution of oxide growth
on Ta (100) in an oxygen ambient

5.2.1. Deconvolution analysis

The Ta4f spectrum after sputter cleaning in the sample preparation chamber is shown in Figure 45. Deconvolution of the data demonstrates the presence of four states that matched the existence of four oxidation states possible by tantalum[62,137]. The peak positions for each state of tantalum are summarized in Table 14. Each state has two unique spin orbit signals corresponding to the $4f_{7/2}$ and $4f_{5/2}$ orbits located 1.9eV from each other.

The spectrum shows a minimal amount of Ta_2O_5 and other suboxides, while metallic tantalum is the dominant component. Deconvolution allows for the measured signal intensity, φ, to be interpreted as the sum of intensity of each oxide state, as shown in equation 9, where n is the valence states of tantalum. The intensity of each oxide state can be referred to as the relative area ratio of each peak with regards to the total area of the Ta4f spectrum. The sum of the signal of these two orbits will be quantified as the total photoemission of each oxide state.

Table 14. Peak positions of components of Ta4f spectrum

Oxide	E_b (eV)		Δ_{SO} (eV)
Ta	21.900	±0.2	1.8±0.05
TaO	23.900	±0.1	1.8±0.06
TaO_2	26.550	±0.2	1.8±0.07
Ta_2O_5	27.45	±0.1	1.8±0.08

$$\varphi_{Ta4f} = \sum_{n=0}^{S} \varphi(Ta_{5/2}^n + Ta_{7/2}^n) \qquad (9)$$
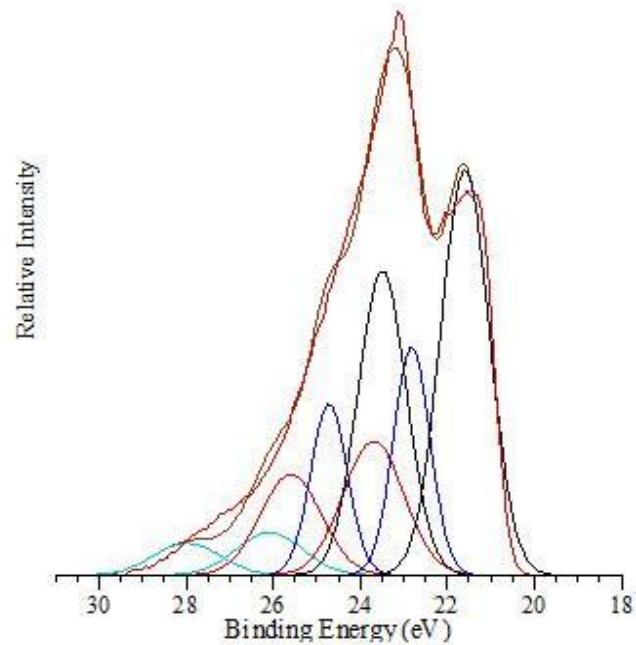
Figure 45. Initial states of Ta4f after sputter etching and prior to *in-situ* oxidation analysis

Oxidation was allowed to continue until a stable condition was obtained. Deconvolution of the final states shows a higher relative area of Ta^0, or un-oxidized tantalum, in the sample with lattice strain, as seen in Figure 46. The causes of this behavior will be described in the following sections.
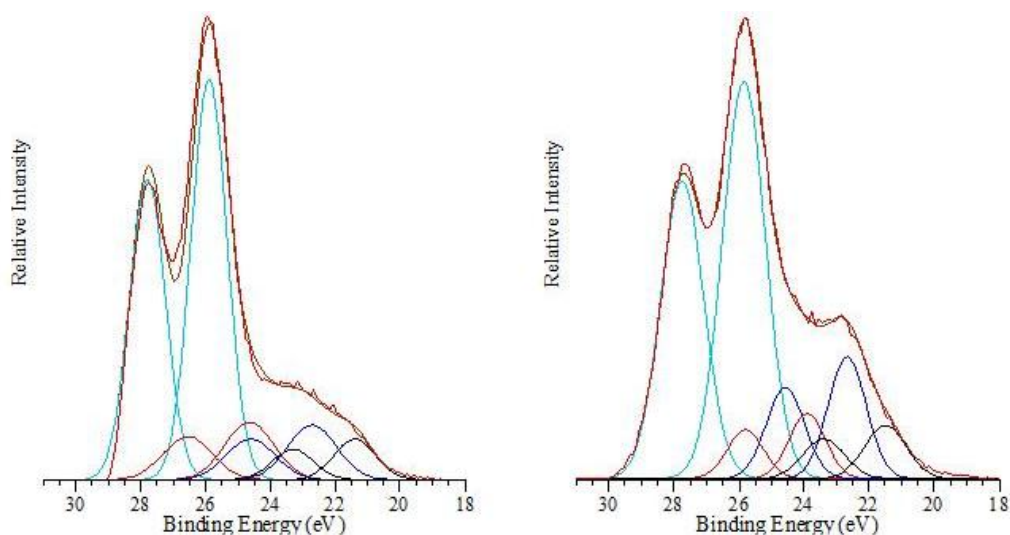
Figure 46. Final oxidation states of the reference tantalum sample (left)
and the lattice-strained sample (right)

5.2.2. Kinetics of mechano-activated oxidation

The deconvolution process shown in the previous section is applied to the temporal evolution surveys similar to those presented in Figure 44. Such analysis can provide insight into the instantaneous evolution of the metal and oxide states during the oxidation process. Activation energy has been previously only been identified for Ta^{+5} since it is considered the lowest energy state and thus the only one been able to measure by the means in this research[138].

The ratio of Ta^{+5} is measured for each time-resolved survey performed *in-situ* during the oxidation process at each temperature, as specified in the methods section. The ratio of Ta^{+5} with respect to the total signal of the Ta4f spectrum is plotted in Figure 47. Of primary importance is the initial growth rate, *k*, upon exposure to an oxygen environment. The growth rate is calculated for the initial quasi-linear growth rate, as shown in the graph.
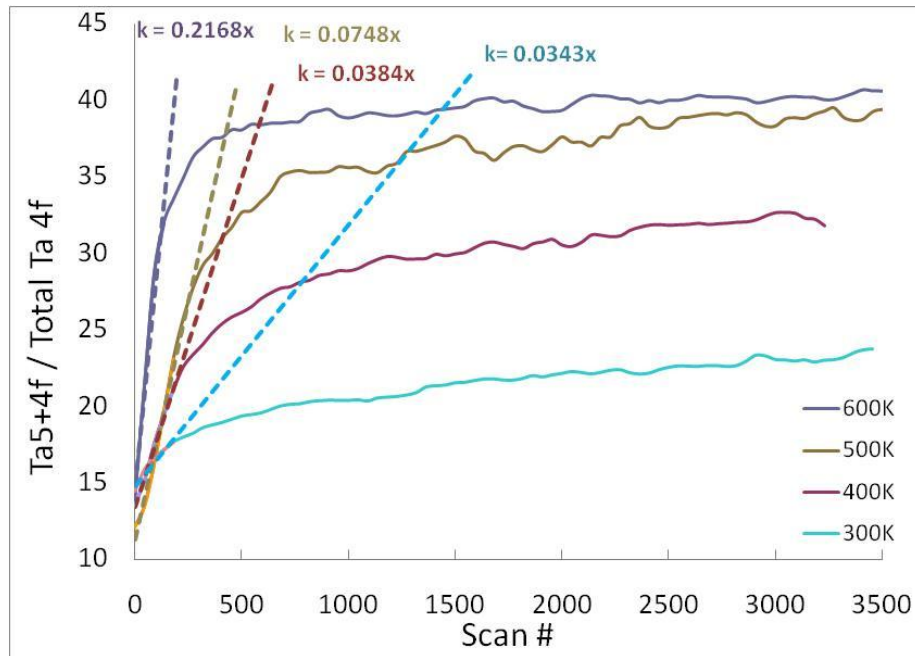
Figure 47. Growth rates of Ta^{+5} during oxidation growth on Ta (100)
reference sample

Arrhenius' equation, presented in equation 10, is a common equation for growth rate and activation energy calculations. To calculate activation energy for each sample, the logarithmic growth rate was plotted against the inverse temperature. The slope of such graph is equal to the activation energy, as presented in equation 11. In this formula, T is absolute temperature, R is the gas constant, E_a is the activation energy, and k is the growth rate of Ta^{5+} during the first growth zone previously mentioned.

$$k = Ae\frac{E_a}{RT} \tag{10}$$

$$\ln k = \ln A \cdot E_a \frac{1}{RT} \tag{11}$$

The activation energy for the tantalum reference sample was calculated to be 8.66KJ/mol (0.089ev/atom) and 12.56KJ/mol (0.12ev/atom) for the strained sample. A summary of the activation energies for the other four samples are presented in Table 15.

Table 15. Activation energies of tantalum samples with different crystallographic orientations and different lattice constraints

Sample Orientation	Activation energy (kJ/mol)		
	Reference	Strained	% change
100	8.656	12.559	45.092
110	4.655	18.560	298.743
111	3.618	11.700	223.370

5.3. Modified Arrhenius' Equation model

The difference in activation energy is attributed to the residual stress previously present at the surface. Effects of microstructural features (defects, boundaries, etc.) can be disregarded since AFM analysis demonstrates an insignificant change in the samples. Previous studies have shown the effects of strain and the chemical reactivity. Strained lattices can vary the chemisorption energy of CO gas onto Cu, Pt, Ni, and other metals [42]. Deposited molecules can self-arrange in unique patterns if the strain causes a large lattice mismatch[44]. The site of chemisorption can also be modified [45]. It has also been found that gas molecules have a preference on a surface with tensile stress than

compressed stress [48,63]. As lattices are placed in compression, bond lengths are disrupted from their equilibrium Lennard-Jones potential position. This disruption changes the energy of the system and changes the activation energy.

Reaction rates do not merely rely on activation energy and temperature as is otherwise indicated by Arrhenius' equation. There are other variables that go unaccounted that can affect the reaction rates. Some of these have been previously reported and include variations in partial pressure of the activating gas [59], bond energy between different metals [60,139], defect and defect concentration[58], and impurities [57]. Two samples whose only difference is one of the aforementioned variants will respond with different reaction rates and appear to have different activation energies. However, when the samples only differ structurally, such as number of defects or boundaries, similar reaction rates will be achieved at a particular temperature. At this temperature, thermal energy and defect energy are near equilibrium and thus appear to cancel the effect of each other. In the plot of the natural logarithm of the reaction rate versus the inverse temperature, the reaction rates for these samples intersect at one point. This point is known as the isokinetic point [140].

In order to account for the effect of variations, Galway [141]describes of a method of adapting the Arrhenius equation to correct kinetic reactions, shown below.

$$k = \beta A e^{\frac{E_{app}}{RT}} \qquad (12)$$

The kinetic correction variable, β, is used to adjust for the empirical deviation from the original equation and has to be calculated for the specific conditions present.

E_{app} is the apparent energy considered under ordinary reactions. This term is referred to as an apparent energy since changes in the reaction rates would result in different activation energy.

In our research, we discovered an additional factor affecting the reaction rate of a single crystal metal. We determined the effect of strain on an otherwise unmodified crystalline structure capable of changing this reaction rate. We account for and predict the effect of mechanical strain of the lattice on the activation energy.

We revise equation 10 to incorporate the effects of thermal and mechanical strain. In order to do this, we begin by arranging the equation to eliminate the pre-exponential factor and function with only temperature and reaction rates.

$$ ln\ k_1 = lnA - \frac{E_a}{RT_1} \tag{13} $$

It is assumed that changes in *A* are negligible with respect to temperature and thus remain constant. Since both samples share an isokinetic point at 600K, we can adapt equation 12 for the isokinetic point and any other point on the activation curve. Temperature is then changed into terms of thermal strain where α is the coefficient of thermal expansion.

$$ E_{app} = \frac{RT_1 T_{iso}}{\Delta T} \ln\left(\frac{k_1}{k_{iso}}\right) \tag{14} $$

$$ E_{app} = \frac{\alpha RT_1 T_{iso}}{\varepsilon_{th}} \ln\left(\frac{k_1}{k_{iso}}\right) \tag{15} $$

Since the degree of thermal strain is affected by the amount of mechanical strain, we can account for mechanical strain such as

$$E_{app} = \frac{\alpha R T_1 T_{iso}}{\varepsilon_{th}\varepsilon_{mech}} \ln(\frac{k_1}{k_{iso}}) \tag{16}$$

We can begin attempt to reconstruct Arrhenius' equation working our way backwards. We arrive at

$$\ln k = \frac{\varepsilon_{th}\varepsilon_{mech}}{\alpha} \ln A - \frac{E_{app}}{RT} \tag{17}$$

which yields

$$\beta = \frac{\varepsilon_{th}\varepsilon_{mech}}{\alpha} \tag{18}$$

as demonstrated in equation 12.

Empirical results of the logarithmic reaction rate versus the inverse temperature for both reference and strained Ta (100) samples are shown in Figure 48. The result for the compressed sample shows a high degree of correlation with the predicted reaction estimated from the model developed here. The same can be seen for the samples of Ta (110) and Ta (111) in Figure 49 and Figure 50, respectively.
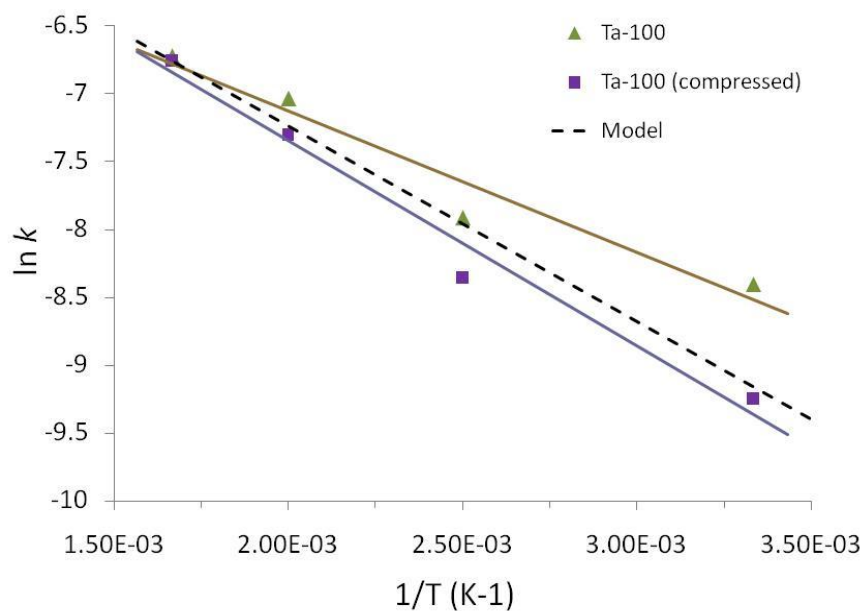
Figure 48. Ta (100) reference and strained empirical values with the modeled reaction obtained from equation 11
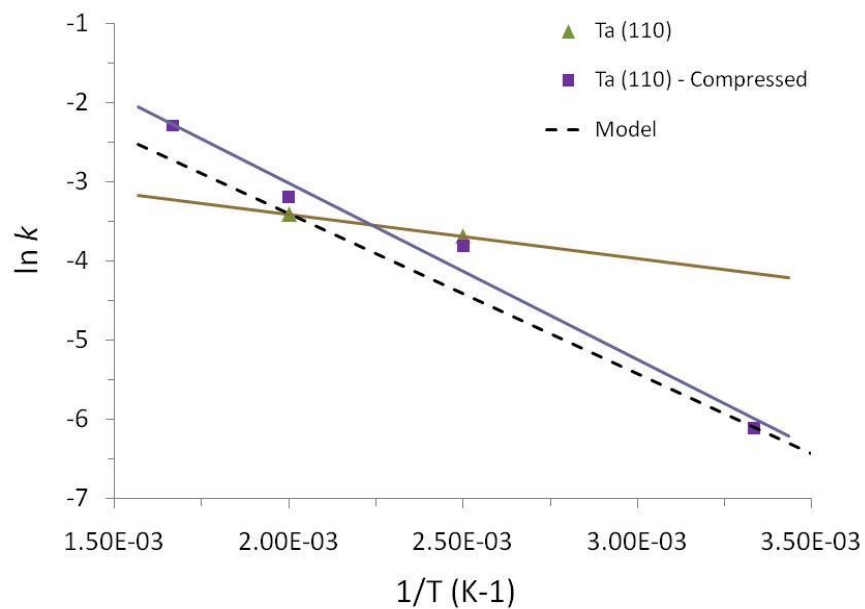
Figure 49. Ta (110) reference and strained empirical values with the modeled reaction obtained from equation 11
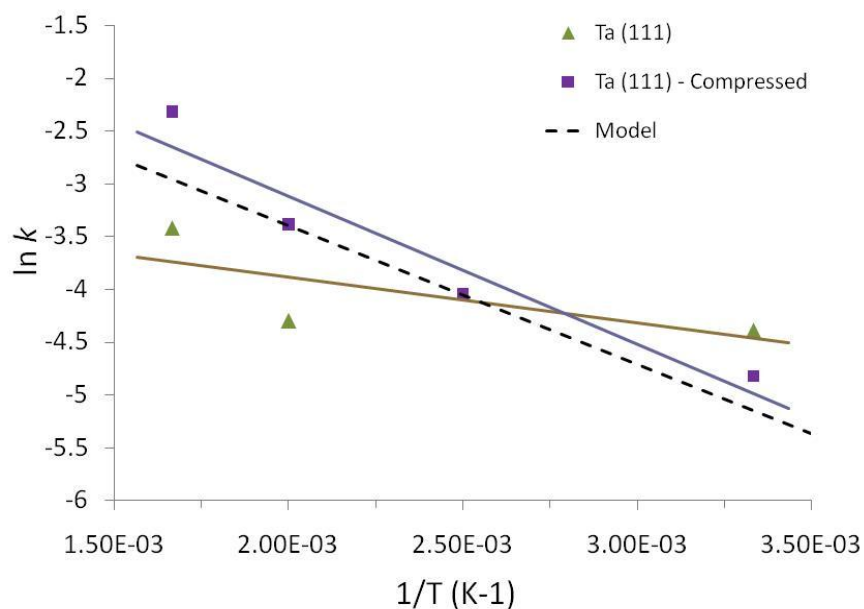
Figure 50. Ta (111) reference and strained empirical values with the
modeled reaction obtained from equation 11

5.4. Summary

Uniaxial compression of a single-crystal tantalum sample produced a residual

stress on the surface which was evident by XRD analysis. Oxidation kinetics with and

without such stress was studied *in-situ* using an ambient pressure XPS. Results showed

that the sample without residual stress produced a greater amount of pentoxide.

Oxidation begun with mixed formation of suboxides and pentoxide, followed by

transformation from suboxides to pentoxide, an equilibrium state product. Furthermore,

a compressive stress was found to increase the activation energy of oxides. This was due

to the reduced lattice spacing resulting the difficulties for oxygen atoms to diffuse and

bind with the metal atoms.

We have seen in this chapter how XRD was used to calculate the strain and residual stress present in the crystal lattices of tantalum single crystal samples. Oxidation at different temperatures was investigated *in-situ* with XPS techniques to obtain a time resolved evolution of the oxidation of tantalum. By measuring the ratio of composition of Ta^{+5} with respect to the entire spectrum, a linear growth rate was calculated. The logarithm of the growth rate was plotted versus the inverse temperature where the slope of the best-fit line gives an accurate measure of the activation energy. Furthermore, the quantified strain in the lattices was incorporated into a new modified activation energy equation to predict the reaction rates of the strained samples. This line was seen in the final figures of this chapter to fit with close resemblance to the empirical values.

CHAPTER VI

MECHANISMS OF OXIDATION UNDER STRESS

Oxidation was monitored using *in*-situ XPS techniques untill a stable condition was achieved. By methods explained in the previous chapters, analysis could be performed on the spectra providing a temporal resolution to the oxidation development. In this chapter we discuss how a strained lattice results in an alteration not only in the activation energy, but also in the final structure of the oxide.

6.1. Stressed oxide growth

During oxidation, tantalum reacts with oxygen creating a blend of suboxides and pentoxide. Our (?) previous studies have shown that tantalum pentoxide is the lowest energy state and most stable state of tantalum[62]. Hence, in an oxidation process, tantalum pentoxide is the most abundant component.

The relative quantity of a particular component is proportional to the signal intensity of that component in the XPS spectrum. The spectrum obtained is a cumulative signal of all the components. That is to say the spectrum signal φ_{Ta4f}, shown in the following equation, is a summation of all the individual signals for each oxide. By deconvoluting each spectrum, we are able to obtain the relative signal intensity of each oxide.

$$\phi_{Ta4f} = \sum_{n \neq 1}^{5} \varphi(Ta_{5/2}^n + Ta_{7/2}^n) \tag{19}$$

The relative signal intensity of tantalum pentoxide is calculated for the spectra shown in Chapter V. The ratio of the pentoxide signal versus the total signal, φ_{Ta4f}, is calculated for each oxidation condition. The ratios of pentoxide, shown as percentages, of the three as-received samples with oxide grown at 600K are shown in Figure 51.

The graph shows a quickly increasing signal ratio of pentoxide in the early stages of oxidation. This implies that pentoxide is becoming a more dominant component on the sample surface. The intensity of the total signal is affected by the inclusion of oxygen during *in-situ* spectroscopic analysis. These variations in total signal intensity affect the relative ratio calculations which cause some degree of noise, seen in the graph.
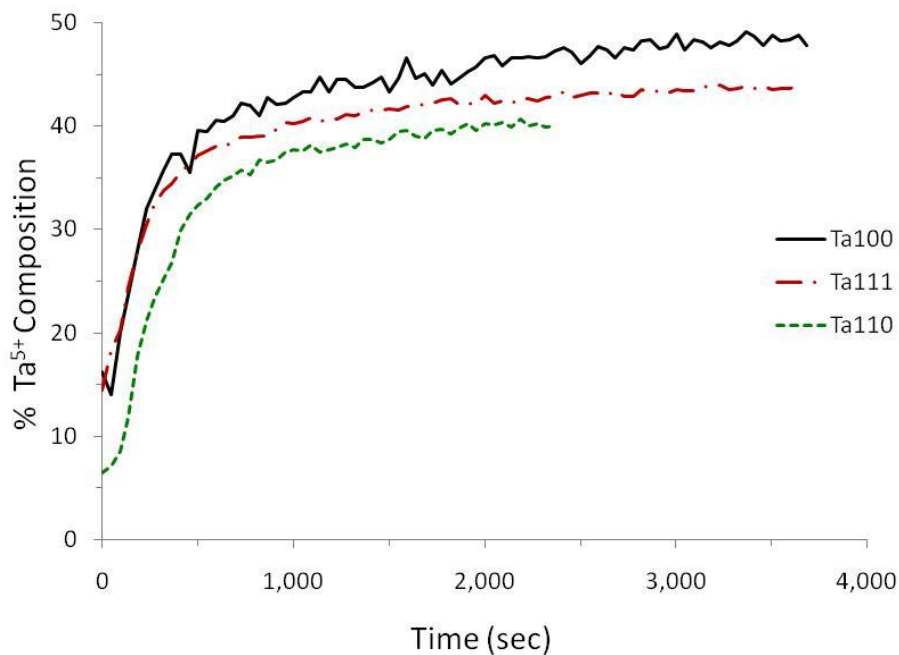
Figure 51. Tantalum pentoxide growth of as-received samples shows
distinct growth ratios for each orientation

Nanoindentation was used to characterize and measure the oxide thickness. A Berkovich diamond tip was used on an MTS nanoindenter under oscillating ramp up load. The oscillating ramp load was capable of providing a depth profile for various properties typically observed via nanoindentation, in particular hardness and modulus of elasticity. Figure 52 shows the hardness depth profile of the three as-received samples after the final oxidation at 600K. The plots shown are the averages of 12 indents on each sample. Figure 53 shows the modulus of elasticity depth profile of the same samples.

The nanoindenter is able to simultaneously and automatically calculate the modulus of elasticity as a function of depth thanks to its oscillating loading scheme explained in Chapter III. The differences in hardness and modulus of elasticity are due to the oxidation mechanisms on the differently oriented substrates[6]. The structure of the oxide depends on the oxidation growth rate which is dependent on temperature, availability of oxidizer, and substrate[142].
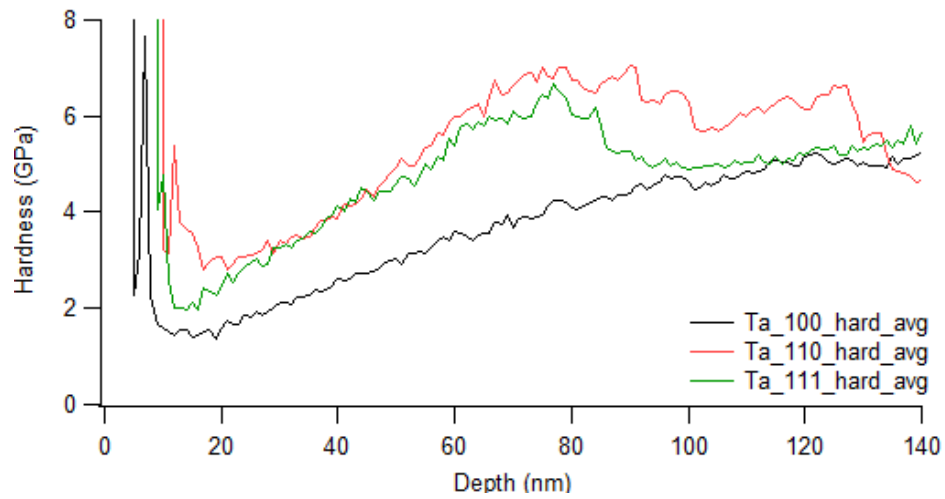
Figure 52. Hardness-depth profiles for as-received samples show
varying maximum peak hardnesses for each crystal orientation
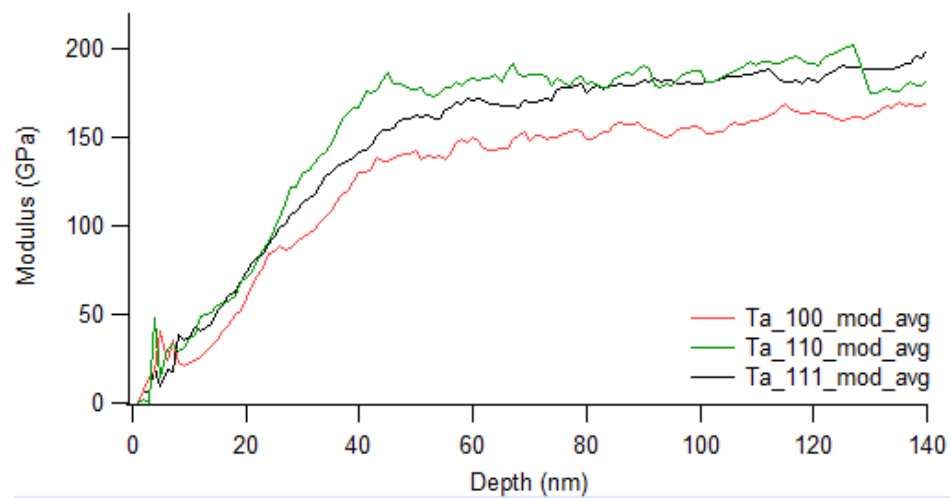
Figure 53. Modulus of elasticity profiles show distinct variance
between the oxides grown on differently oriented tantalum crytsals

The oxide film thickness was calculated via the nanoindentation loading rate using a published method[143-145]. The first derivative of the load on the sample is calculated, as shown in Figure 54 for the compressed Ta (100) sample. The top plot shows the first derivative of the load shown on the bottom. A sudden distortion of the first derivative occurs at 58.2nm from the surface of the sample. This is the depth of a material property change related to an interface of two materials, the oxide and metal. Distortion seen of the first derivative at the maximum penetration depth is due to a load hold for creep control and unloading of the tip and should be disregarded for the purpose of this investigation. Similar plots for the (110) and (111) samples show a thickness of 94.7nm and 68.7nm, respectively. A comparison with the compressed samples will be presented shortly.
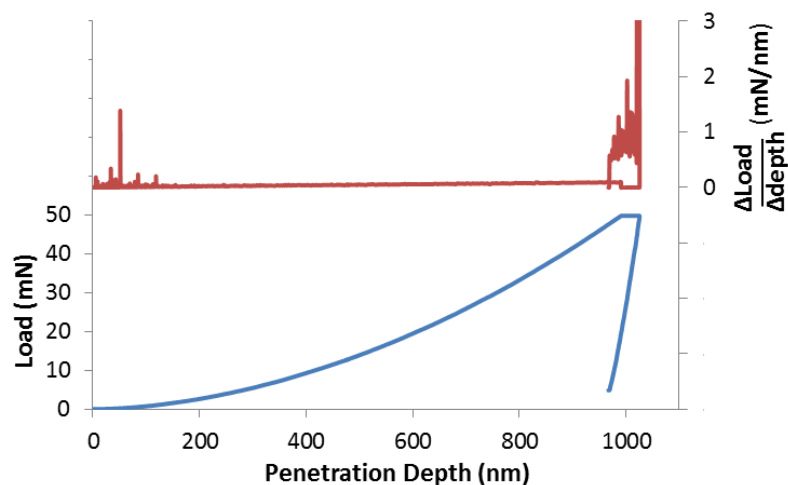
Figure 54. Loading of nanoindenter tip vs depth on bottom and first derivative of loading curve on top. First derivative indicates a change in the loading rate which is where the tip encounters an interface between two different materials

Similar analysis was performed on the stressed lattice samples which have also undergone oxide growth at 600K. The instantaneous ratio of pentoxide during growth, as monitored by XPS, is displayed in Figure 55. It is immediately evident that for the stressed conditions, there appears to be no distinction in the pentoxide composition for any sample, as was the case for the as-received samples. In the stressed samples, pentoxide growth is seen to initially develop linearly at an equal rate. The three growth rates then transition into a less rapid linear growth, though the time for this transition occurs at different points. More on this will be discussed in the following sections.
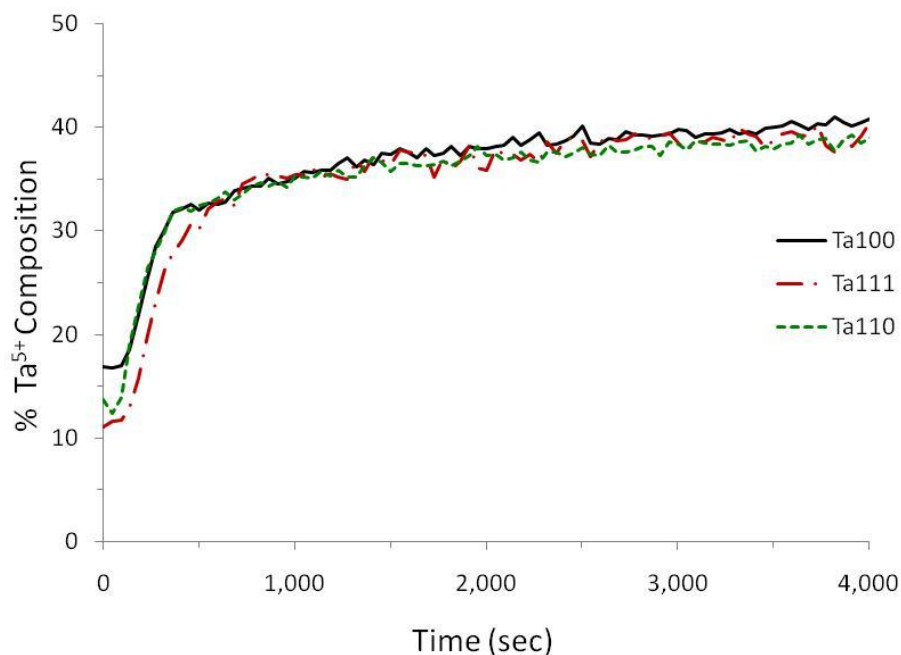
Figure 55. Stressed-lattice samples show a similar ratio of tantalum
pentoxide growth during in-situ oxidation

Nanoindentation studies on the oxide developed on the stressed samples were performed in similar methods as for the as-received samples. A depth profile of the

oxide hardness for each of the compressed samples is shown in Figure 56. A depth

profile of the modulus of elasticity is shown in Figure 57. As with the pentoxide growth,

there is no apparent distinction in the hardness of the oxides grown on either sample.
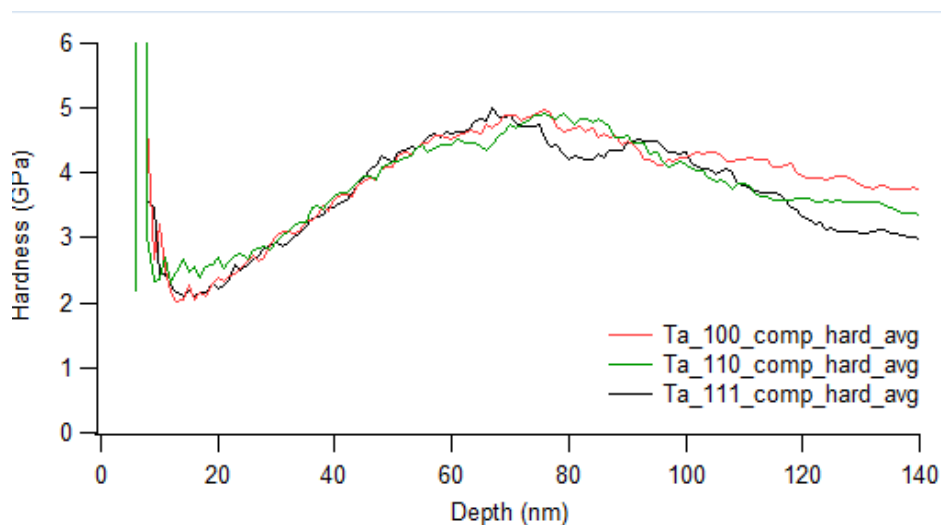
Figure 56. The oxides grown on compresed-lattice samples show
almost identical hardness profiles indicating that the oxide thickness
and structure is similar in all samples
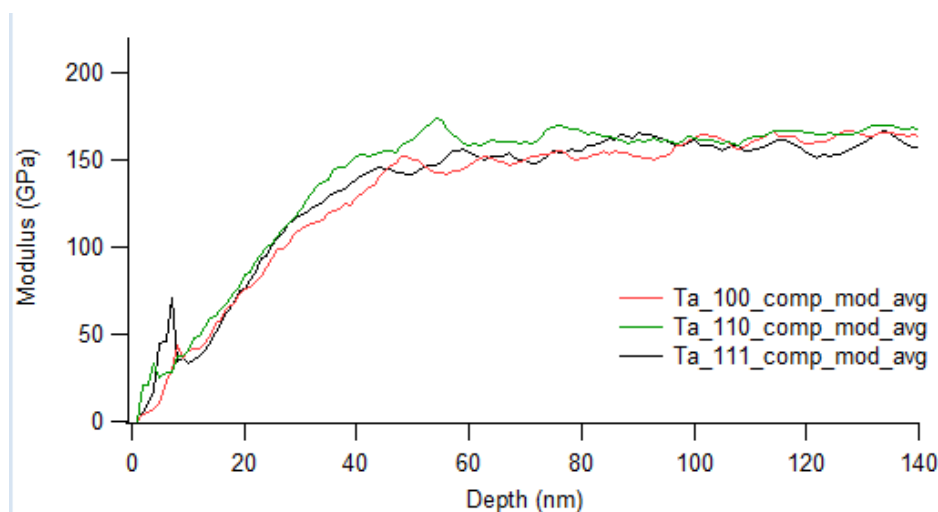
Figure 57. Modulus of the compressed-lattice oxide shows a high
degree of uniformity amongst all samples despite crystal orientation

By performing a similar first-derivative calculation of the load versus penetration depth as performed for the as-received samples, the oxide thickness is calculated for the compressed samples. A comparison of the as-received and compressed samples' oxide thickness is shown in Table 16. When compared to Table 13, it becomes evident that sample (110) which had the highest surface stress, also had the highest change in oxide thickness and vice versa for the (100) sample. The same trend is true when compared with the activation energies shown in Table 15.

Table 16. Oxide thickness of as-received and compressed samples as measured by the first derivate of the load on the sample

	Oxide Thickness (nm)		
Sample	As-received	Compressed	% change
100	58.173	58.827	0.011
110	94.655	51.632	0.455
111	68.683	53.708	0.218

The apparent similitude in the pentoxide ratio, hardness, and modulus of the compressed samples would indicate that the reactive surfaces of the samples have become similar in structure. However, this is not true as evident from XRD analysis shown in the previous analysis. A further investigation is needed in the oxide growth dynamics to understand what may be causing such similar oxide structures.

Oxide formation is dependent on the availability of metal ions to be readily reacted with oxygen and the ease of oxygen to diffuse through the oxide coating to react

with the metal ions[146-148]. Assuming that there is an abundance of oxygen ions, an oxide film would continue growing until all the metal ions were consumed[149]. However, as diffusivity through the oxide film becomes more tortuous, oxidation rates begin to follow a linear-parabolic growth rate[150]. In this assumption, the growth rate transitions from chemical reaction rate to oxygen availability[151].

6.2. Spectroscopic analysis

The crystalline structure of the tantalum samples remains intact after compression. It has been shown from XRD that the lattices of the crystal have been strained and thus exhibit a degree of deformation. An attempt at understanding the relationship between stress and oxide thickness is presented here via spectroscopic studies of the oxide.

As the formation of oxide, the chemical reaction causes a shift of the oxide peak [64,138]. Our results showed that the range of the peak shift was dependent on the strain of the crystal lattice (both mechanical and thermal strain). Oxidation transformation, i.e., the transition between oxides, of the pentoxide for each sample was evaluated by the shift of its corresponding peak as discussed below.

The stressed and as-received Ta (100) samples were oxidized and the data was deconvoluted, as explained in Chapter III. At higher temperatures, it has been reported that oxidation took place faster and produced a more porous oxide film than those at low temperatures [152]. The high porosity of a film allows for a less tortuous path for oxygen ions, enabling them to penetrate into the metal through a thicker oxide film. A

less dense oxide film would also allow for a more thorough metal transformation to oxide[153]. By these two factors, it is to be expected that the 600K samples shift rate is higher than that at 300K. This will indeed be shown in phase images discussed in section 6.3.
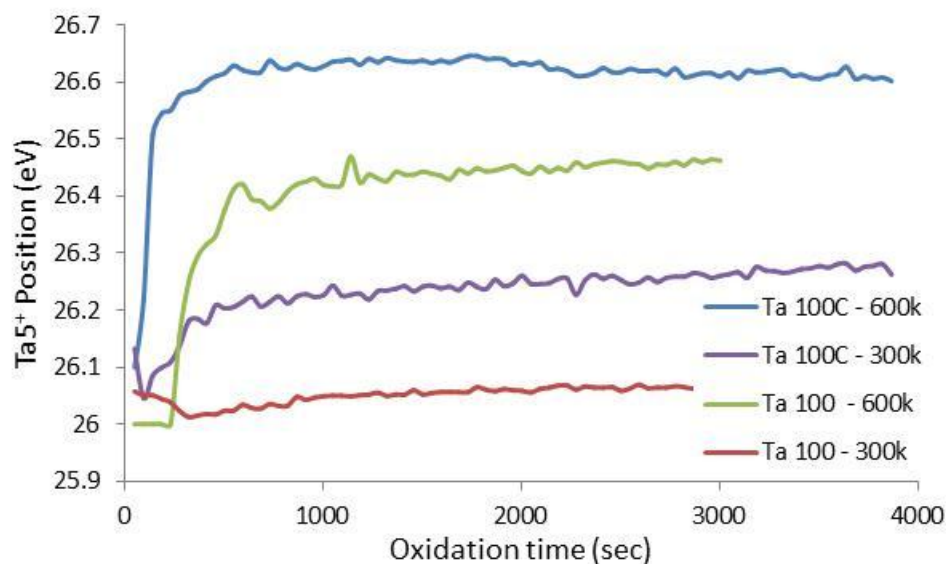
Figure 58. Tantalum pentoxide shifts during oxide growth due to the chemcial changes occuring. This shift is more extensive at higher temperatures and for the compressed samples

The position of the pentoxide peaks is plotted in Figure 58 for the oxides grown at 300K and 600K. The plot shows a larger peak shift rate for the as-received sample at 600K than the as-received sample at 300K. This greater shift at 600K is expected due to a higher amount of energy in the system allowing a greater amount of metal ions to be converted.. The compressed samples of the same orientation show a similar trend.
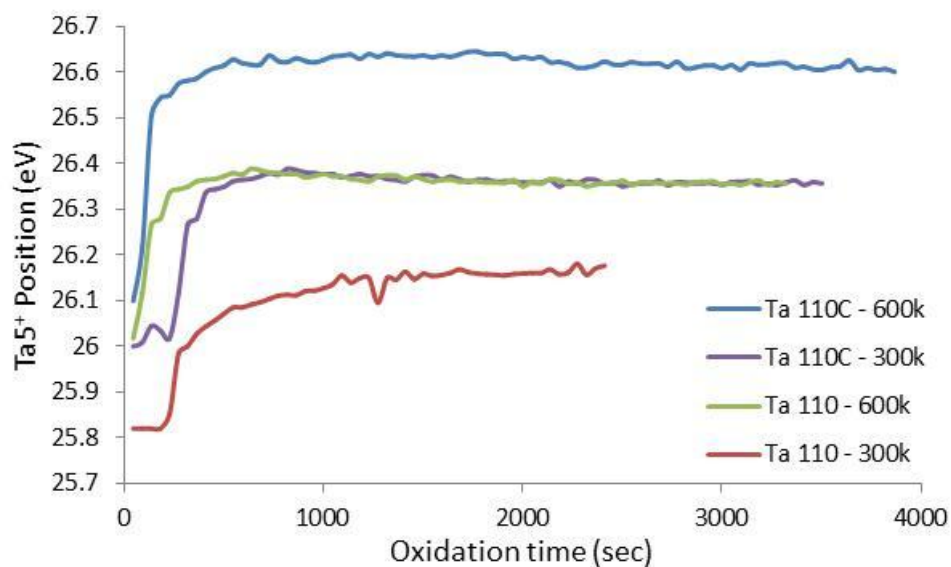
Figure 59. Tantalum (110) compressed samples show a higher peak shift of he tantalum pentoxide at higher temperatures and compressed lattices
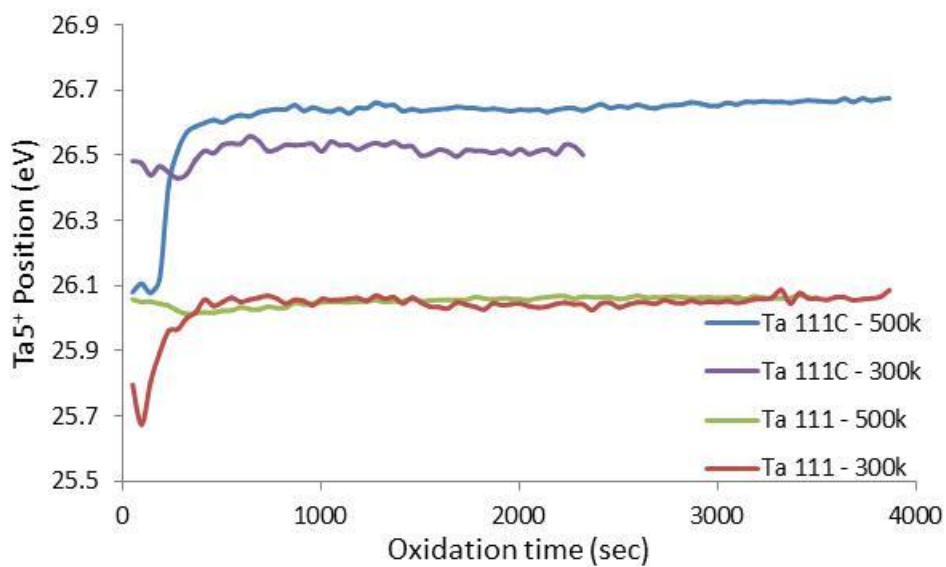
Figure 60. Tantalum (111) samples show a higher peak shift of pentoxide at higher temperatures and stress states

The trend is repeated for the samples with a (110) and (111) orientation, as seen in Figure 59 and Figure 60 respectively. The final peak position of the samples with oxide at 300K is summarized in Table 17 and with the percent difference of the final peak position.

Table 17. Maximum peak shift for tantalum pentoxide at 300K

Sample Orientation	As-received (eV)	Compressed (eV)	% Peak Difference
100	26.055	26.248	0.742
110	26.157	26.364	0.791
111	26.043	26.499	1.751

The peak shift is more evident for the samples with oxide at 600K, which are summarized in Table 18. The percent difference in the peak position at the end of the oxidation process is calculated and displayed as well.

Table 18. Maximum peak shift for tantalum pentoxide at 600K

Sample Orientation	As-received (eV)	Compressed (eV)	% Peak Difference
100	26.436	26.611	0.662
110	26.354	26.610	0.971
111	26.064	26.647	2.236

Comparing the percent peak position calculated in Table 17 and Table 18 with the surface strain calculated in Table 12, we see a linear relationship between surface strain and peak shift, as shown in Figure 61. At higher strain, samples exhibit a decrease in peak shift. Also, at higher strain, temperature plays a lesser effect in the amount of peak shift, as evident by the convergence of the 300K and 600K shifts at higher strain.
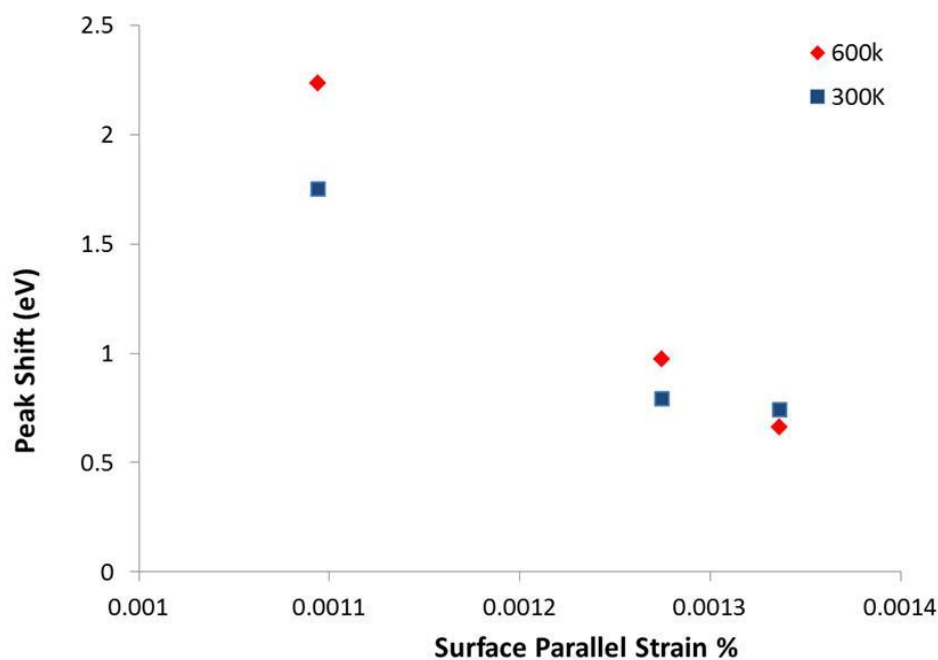
Figure 61. Peak shift shows a linear trend with surface strain

At lower strain, the oxide is less restricted in the chemical bonding created, forming an oxide structure based on the substrate and thus causing differences in the oxide properties, as shown in the nanoindentation results. At higher strain, samples are

constrained during oxidation, as indicated by a constraint in the peak shift. At this region, substrate structure plays a lesser effect on oxide structure, as shown by the nanoindentation properties of the compressed samples. The similarities in oxide thickness and mechanical properties become similar at higher strain indicating the dominant effect of strain.

6.3. Oxidation kinetics

The final percent content of Ta^{5+} of the as-received samples is lower than the compressed samples at the same temperature. It is known that oxidation generally continues until the diffusion of the oxidizer becomes inhibited by its oxide layer [154]. The process is then unable to transport oxygen molecules through the oxide. The phase images taken by AFM methods shown in Figure 62 show a uniformly structured oxide for the as received samples on the left column. The corresponding compressed samples show a discontinuous structure. Interfacial features, such as different structures of oxide, provide a method for oxygen moleculs to reach the metal surface when the oxide has become too thick. The evolution and transformation of oxides are essential to understand effects of strain on oxidation.
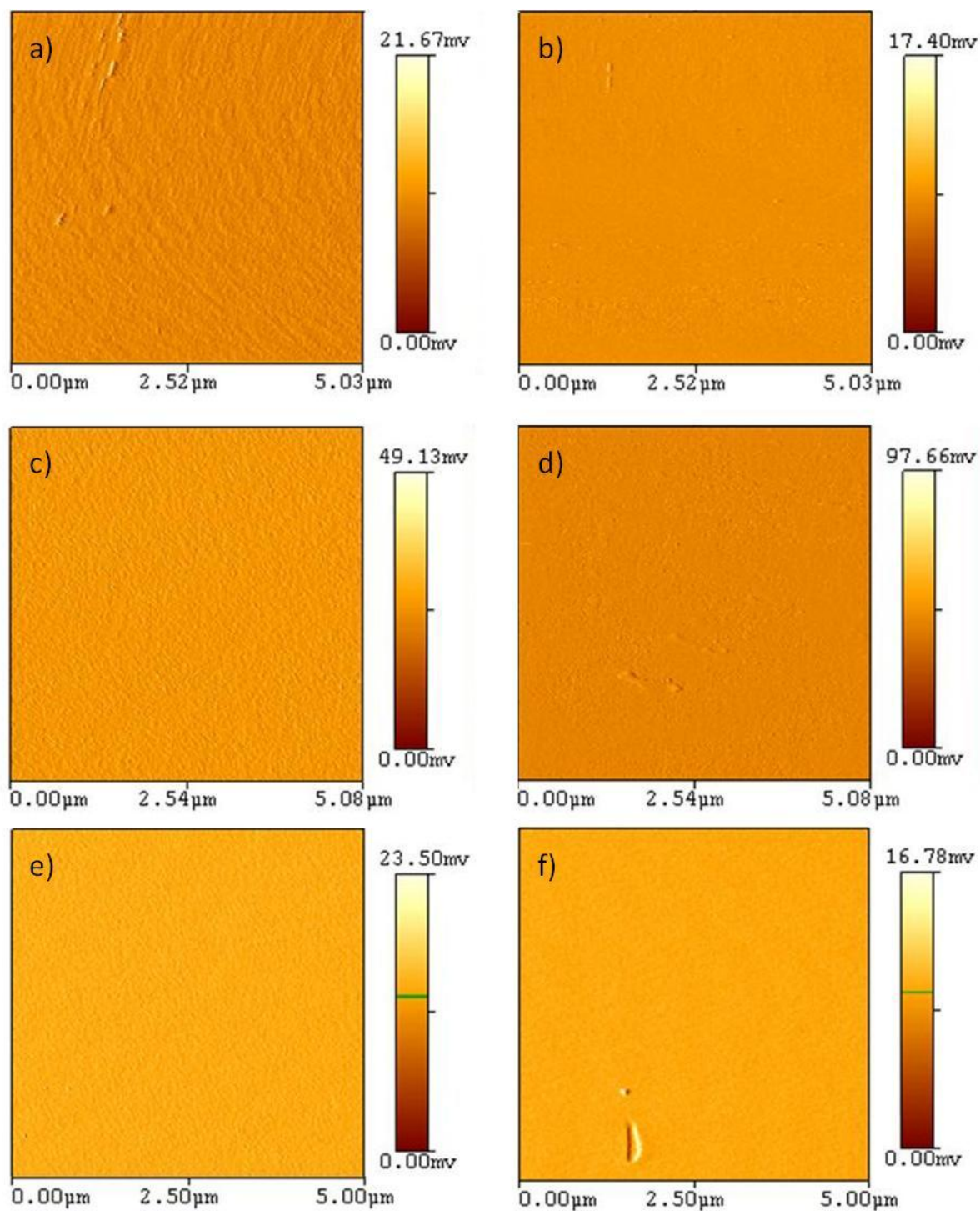
Figure 62. Phase images of oxide as developed on a) Ta (100) as-received, b) Ta(100) compressed, c) Ta(110) as-received, d) Ta(110) compressed, e) Ta(111) as-received, f) Ta(111) compressed

It has been reported that the evolution of $Ta^{5+}4f$ at 300K shows three

identifiable regions: metal oxidation, mixed-oxidation, and suboxide transformation[64]. In

this research, this is seen in the as-received sample as shown in Figure 63. The first

region is distinguished by a linear growth that lasts about 300 seconds. This region is

dominated by a rapid Ta^{5+} growth formed mostly from Ta^0. The next region is a mixture

of metal and suboxide transformation into Ta^{5+} and follows a logarithmic growth. After

270 seconds, the growth becomes linear and is dominated by a transition from Ta^{2+} to

Ta^{5+} until a stable condition is met. A similar trend is seen for the case of pentoxide

grown at 600K on the as-received and compressed, Figure 64 and Figure 65,

respectively. A summary of the starting time for each stage is presented in Table 19.
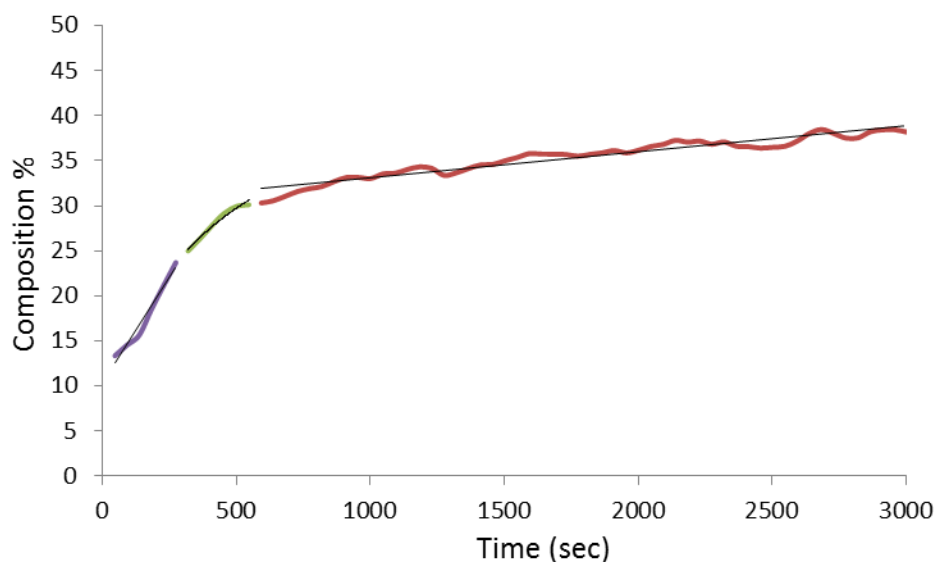
Figure 63. Ta (100) oxidation at 300K shows three distinct regions of
oxide transformation
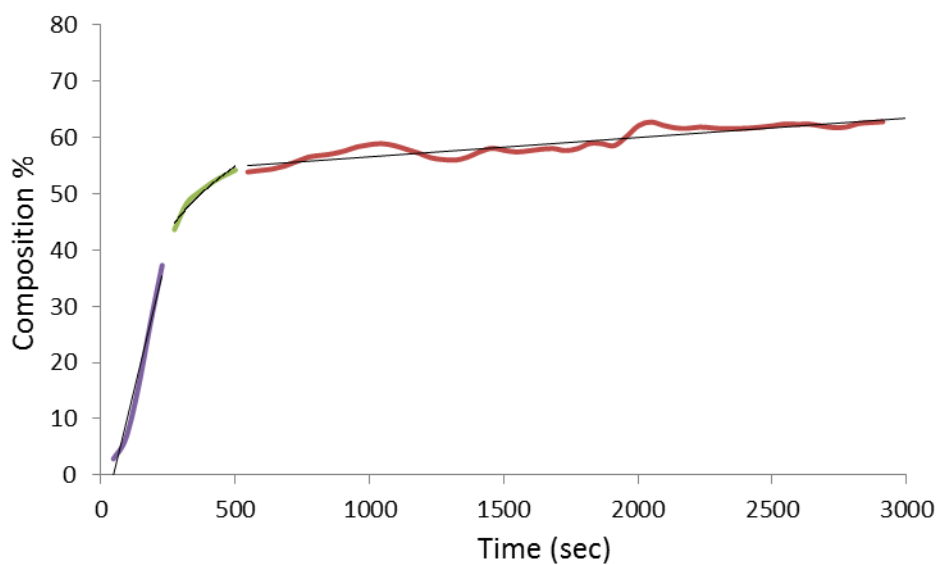
Figure 64. At 600K, Ta (100) shows three growth mechanisms
dominated initially by a linear growth, a logarithmic transition, and
finishing in linear manner
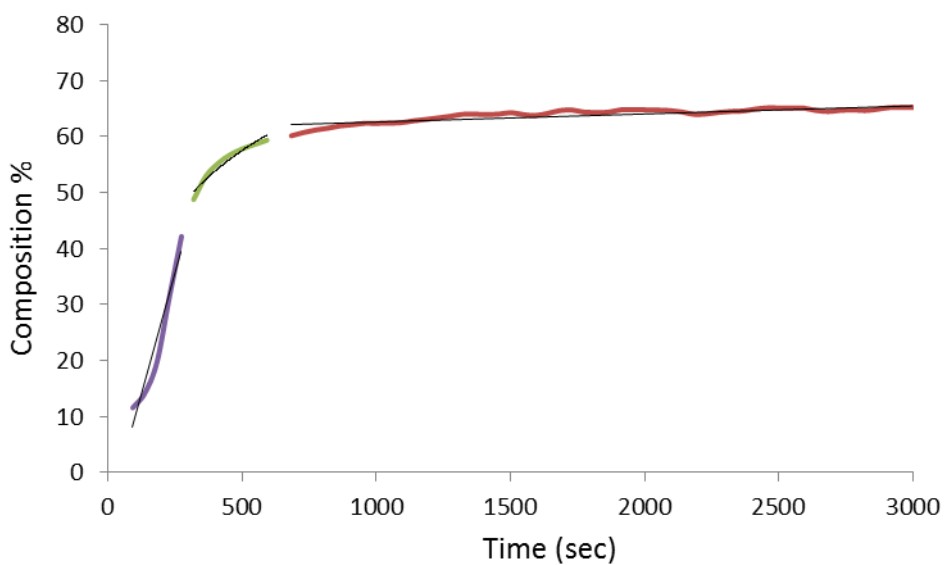
Figure 65. The compressed Ta (100) at 600K shows a longer transition
stage than the as-received sample at same temperature

Table 19. Stage duration for each form of oxide transformation

Sample	Temp	Condition	Stage 1 Duration (sec)	Stage 2 Duration (sec)
100	300	As-received	318	273
		Compressed	228	217
	600	As-received	273	273
		Compressed	319	363
110	300	As-received	227	91
		Compressed	-	-
	600	As-received	364	227
		Compressed	182	182
111	300	As-received	227	183
		Compressed	227	227
	600	As-received	318	319
		Compressed	91	273

Oxidation of tantalum pentoxide has been simplified to be modeled by the equation shown below, where D_T is the tantalum pentoxide diffusivity, D_S is the substrate diffusivity, y is the Ta2O5 thickness and y' is the substrate 'consumed' thickness[52].

$$\frac{D_T}{D_S} = \frac{y}{y'}$$ (20)

This model does not incorporate crystallinity and grain boundaries for poly-crystalline substrates. The Deal-Grove model of oxidation has been shown as an accurate

method of predicting silicon oxide growth[155] by calculating growth factors from empirical data. This model has been shown to be able to be modified for other types of oxide growth[156], and can be considered for this experiment. The Deal-Grove predicts oxide thicknes, x, as shown below.

$$x^2 + Ax = B(t + \tau) \tag{21}$$

where

$$A = 2 * D_{eff}(\frac{1}{k} + \frac{1}{h}) \tag{22}$$

and

$$B = 2 * D_{eff}C^*/N \tag{23}$$

where D_{eff} corresponds to the effective diffusion of the oxide, k is the growth rate, h is the gas-phase transport coefficient, C^* is the equilibrium concentration of the oxidant in the oxide, and N is the number of oxidant molecules incorporated into a unit volume of the oxide. B is known as the parabolic growth rate and B/A is the linear growth rate. Growth of silicon oxide undergoes a similar transition of competing oxidation mechanisms; i.e., reaction limited and diffusion limited[157]. During the initial stages of oxidation, the oxide grows at an exponential rate until a certain thickness is achieved. The oxide rate then becomes linear until all silicon is consumed. However, as can be seen in from the last graphs shown, growth cedes to continue after the logarithmic transformation occurs. Alterations of the Deal-Grove model have been suggested for

oxides that cede to grow after the exponential growth. . The Deal-Gove equation shown previously has been reduced to only the exponential form shown below. [158]

$$x^2 = Bt \qquad (24)$$

The parabolic rate constant, B, is typically evaluated by empirical results from oxidation growth at different temperatures. We see that the definition of B shown is described as being strictly a function of the oxide structure and not the substrate conditions. The results presented in this chapter show that this simplification fails to account for surface stress and crystal orientation. The growth rate is affected by crystal orientation and surface stress. For this reason, it is expected that this value has to be modified such that:

$$B = 2 * D_{eff}C^*/N * f(\varepsilon_{mech}, \Psi) \qquad (25)$$

CHAPTER VII

CONCLUSION AND FUTURE RECOMMENDATION

7.1. Conclusions

This research was focused on studying the effects of mechanical activation of reactive surfaces. Experimental analysis was performed on a naturally produced lubricant extracted from cockroaches and on single crystal tantalum. The effects of mechano-activation were studied for both substances, studying the behavior of a lubricant on material wear debris and the behavior of a metal oxidation with a strained lattice.

The following are highlights of major results and discoveries:

1. It was found that the naturally produced lubricant reacted with wear debris from a stainless steel sample when mechanically activated during tribological tests. This reaction resulted in a decrease in the binding energy of iron, as investigated by various x-ray spectroscopy methods. It was shown that this change in binding energy was a result of the formation of an organo-metallic alloy.

2. It was found that single crystal tantalum samples had a changed activation energy proportional to a strain in the crystal lattice. More so, a mathematical model was created to account for the crystal strain in determining the activation energy of tantalum. This is a first step in determining and predicting how a material will behave when exposed to strain at the lattices.

Until now, studies had only investigated the extent of the effects of strain but had fallen short in attempting to mathematically predict the extent.

3. It is shown that strain can become a major component in the structural formation of an oxide. At low strain, the oxide structure is dependent on the substrate. At higher strain, the substrate becomes less relevant in the structure of oxide. This is shown by a similitude in oxide properties on samples with high strain. The higher strain limits the ability for a chemical bond to develop, as evident by a reduction in the peak shift of strained samples. The constraint of the peak shift due to lattice strain begins to explain *why* strain changes the kinetics and dynamics of oxidation.

This research expands the study of material activation by presenting an insight into methods of mechano-activated processes. Materials and reactions can be tailored and tuned to obtain desired properties. Better understanding of variances in common industrial processes could be obtained by further expanding these studies.

7.2. Future recommendations

There remain several variables yet to be investigated for mechano-chemical activation. The author of this research proposes a continuation and expansion of these studies to improve our understanding of mechano-chemical activation on a wider scale. For one, the research presented in the lubricant chapter was limited to one natural wax. It

would be of interest to study how different waxes with different compositions and molecular weights behave to mechanical activation.

Secondly, studies on oxidation of strained-lattice metals should be continued on a diverse range of metals to obtain a more solidified theory of the effects of strain. An expanded knowledge of strain/stress induced activation variations could help explain many industrial challenges.

REFERENCES

[1] E. Eliav, U. Kaldor, and Y. Ishikawa, Physical Review Letters **74,** 1079 (1995).

[2] A. B. Anderson and R. Hoffmann, Journal of Chemical Physics **60,** 4271 (1974).

[3] B. Beckhoff, N. Langhoff, B. Kanngiefer, R. Wedell, and H. Wolff, *Handbook of practical X-ray fluorescence analysis* (Springer, New York, 2006).

[4] Y. Cauchois, *Les spectres de rayons X et la structure électronique de la matière.*, Vol. 5 (Centre national de la recherche scientifique, Paris, 1948).

[5] N. F. Mott and H. Jones, *The theory of the properties of metals and alloys* (General Publishing Company, Toronto, 1958).

[6] W. Zahn, S. Oswald, A. Fülle, D. Hildebrand, M. Zier, and K. Wetzig, Physica Status Solidi (c) **4,** 1830 (2007).

[7] M. Zier, S. Oswald, R. Reiche, and K. Wetzig, Microchimica Acta **156,** 99 (2006).

[8] M. Buttiker, E. P. Harris, and R. Landauer, Physical Review B **28,** 1268 (1983).

[9] P. B. Visscher, Physical Review B **14,** 347 (1976).

[10] P. Hanggi and F. Mojtabai, Physical Review A **26,** 1168 (1982).

[11] E. H. Rezayi and H. Suhl, Physical Review Letters **45,** 1115 (1980).

[12] A. P. Mills and L. Pfeiffer, Physical Review Letters **43,** 1961 (1979).

[13] A. P. Mills Jr, Solid State Communications **31,** 623 (1979).

[14] J. T. Randall and M. H. F. Wilkins, Proceedings of the Royal Society of London. Series A. Mathematical and Physical Sciences **184,** 365 (1945).

[15] A. Halperin and A. A. Braner, Physical Review **117,** 408 (1960).

[16] J. Luo, L. Han, N. N. Kariuki, L. Wang, D. Mott, C.-J. Zhong, and T. He, Chemistry of Materials **17,** 5282 (2005).

[17] J. Luo, V. W. Jones, M. M. Maye, L. Han, N. N. Kariuki, and C.-J. Zhong, Journal of the American Chemical Society **124,** 13988 (2002).

[18] S. L. Murov, I. Carmichael, and G. L. Hug, *Handbook of photochemistry* (Marcel Dekker, New York, 1993).

19   S. Kundu, K. Wang, and H. Liang, Journal of Physical Chemistry C **113,** 134 (2008).

20   S. Kundu, K. Wang, D. Huitink, and H. Liang, Langmuir **25,** 10146 (2009).

21   S. Eustis, H.-Y. Hsu, and M. A. El-Sayed, Journal of Physical Chemistry B **109,** 4811 (2005).

22   S. Eustis and M. A. El-Sayed, Journal of Physical Chemistry B **110,** 14014 (2006).

23   F. Gao and H. Liang, Journal of the Electrochemical Society **156,** H80 (2009).

24   D. Huitink, F. Gao, and H. Liang, Scanning **32,** 336 (2010).

25   F. Gao and H. Liang, Electrochimica Acta **54,** 6808 (2009).

26   H. Lounici, D. Belhocine, H. Grib, M. Drouiche, A. Pauss, and N. Mameri, Desalination **161,** 287 (2004).

27   H. Lee, R. Cooper, K. Wang, and H. Liang, Sensors **8,** 7359 (2008).

28   T. Jee, H. Lee, B. Mika, and H. Liang, Tribology Letters **26,** 125 (2007).

29   K. Wang, H. Lee, R. Cooper, and H. Liang, Applied Physics A: Materials Science & Processing **95,** 435 (2009).

30   S. Mani, R. Perez, H. Lee, Z. Ounaies, W. Hung, and H. Liang, Journal of Tribology **129,** 836 (2007).

31   H. Lee, R. Cooper, B. Mika, and H. Liang, ASME Conference Proceedings **2007,** 893 (2007).

32   A. Smekal, Naturwissenschaften **30,** 224 (1942).

33   P. Y. Butyagin, Russian Chemical Reviews **53,** 1025 (1984).

34   A. Z. Juhász, Colloids and Surfaces A: Physicochemical and Engineering Aspects **141,** 449 (1998).

35   Z. A. Juhász, Particulate Science and Technology: An International Journal **16,** 145 (1998).

36   K. Wang, S. Kundu, H. Lee, and H. Liang, Journal of Physical Chemistry C **113,** 8112 (2009).

37   M. M. Caruso, D. A. Davis, Q. Shen, S. A. Odom, N. R. Sottos, S. R. White, and J. S. Moore, Chemical Reviews **109,** 5755 (2009).

38   D. R. Rottach, J. G. Curro, G. S. Grest, and A. P. Thompson, Macromolecules **37,** 5468 (2004).

39   D. R. Rottach, J. G. Curro, J. Budzien, G. S. Grest, C. Svaneborg, and R. Everaers, Macromolecules **39,** 5521 (2006).

40   R. Koch, D. Winau, A. Führmann, and K. H. Rieder, Vacuum **43,** 521.

41   R. Abermann, Vacuum **41,** 1279 (1990).

42   M. Mavrikakis, B. Hammer, and J. K. Nørskov, Physical Review Letters **81,** 2819 (1998).

43   J. A. Rodriguez and D. W. Goodman, Science **257,** 897 (1992).

44   T. E. Madey, C. H. Nien, K. Pelhos, J. J. Kolodziej, I. M. Abdelrehim, and H. S. Tao, Surface Science **438,** 191 (1999).

45   J. J. Boland, Surface Science **261,** 17 (1992).

46   E. Kampshoff, E. Hahn, and K. Kern, Physical Review Letters **73,** 704 (1994).

47   M. W. Wu and H. Metiu, The Journal of Chemical Physics **113,** 1177 (2000).

48   M. Gsell, P. Jakob, and D. Menzel, Science **280,** 717 (1998).

49   S. Boughaba, M. Islam, J. P. McCaffrey, G. I. Sproule, and M. J. Graham, Thin Solid Films **371,** 119 (2000).

50   R. Chandrasekharan, I. Park, R. I. Masel, and M. A. Shannon, Journal of Applied Physics **98,** 114908 (2005).

51   J. P. Chang, M. L. Steigerwald, R. M. Fleming, R. L. Opila, and G. B. Alers, Applied Physics Letters **74,** 3705 (1999).

52   C. Chaneliere, J. L. Autran, R. A. B. Devine, and B. Balland, Materials Science and Engineering: R: Reports **22,** 269 (1998).

53   N. Novkovski, A Paskaleva, and E Atanassova, Semiconductor Science and Technology **20,** 233 (2005).

54   H. Iwai, H. S. Momose, M. Saito, M. Ono, and Y. Katsumata, Microelectronic Engineering **28,** 147 (1995).

55   B. W. Shen, I.-C. Chen, S. Banerjee, G. A. Brown, J. Bohlman, P.-H. Chang, and R. R. Doering, in *International Electron Devices Meeting*, Washington, D.C., 1987 (IEEE Publications), p. 582

56   H. Shinriki and M. Nakata, IEEE Transactions on Electron Devices **38,** 455 (1991).

57   J. R. MacCallum and M. V. Munro, Thermochimica Acta **203,** 457 (1992).

58   D. Dollimore and P. F. Rodgers, Thermochimica Acta **30,** 273 (1979).

59   J. Pysiak, Thermochimica Acta **148,** 165 (1989).

60   K. Muraishi and H. Yokobayashi, Thermochimica Acta **209,** 175 (1992).

61   P. Kar, K. Wang, and H. Liang, Electrochimica Acta **53,** 5084 (2008).

62   P. Kar, K. Wang, and H. Liang, Electrochemical and Solid-State Letters **11,** C13 (2008).

63   P. Jakob, M. Gsell, and D. Menzel, The Journal of Chemical Physics **114,** 10075 (2001).

64   G. Ketteler, D. F. Ogletree, H. Bluhm, H. Liu, E. L. D. Hebenstreit, and M. Salmeron, Journal of the American Chemical Society **127,** 18269 (2005).

65   M. Salmeron and R. Schlögl, Surface Science Reports **63,** 169 (2008).

66   M. E. Grass, P. G. Karlsson, F. Aksoy, M. Lundqvist, B. Wannberg, B. S. Mun, Z. Hussain, and Z. Liu, Review of Scientific Instruments **81,** 053106 (2010).

67   H. Bargel, K. Koch, Z. Cerman, and C. Neinhuis, Functional Plant Biology **33,** 893 (2006).

68   A. C. Chibnall, S. H. Piper, A. Pollard, E. F. Williams, and P. N. Sahai, Biochemistry Journal **28,** 2189 (1934).

69   E. H. Dusham, Journal of Morphology **31,** 563 (1918).

70   J. W. L. Beament, Journal of Experimental Biology **32,** 514 (1955).

71   J. A. Ramsay, Journal of Experimental Biology **12,** 373 (1935).

72   V. B. Wigglesworth, Journal of Experimental Biology **21,** 97 (1945).

73   J. W. L. Beament, Journal of Experimental Biology **36,** 391 (1959).

74   J. W. L. Beament, Journal of Experimental Biology **21,** 115 (1945).

75   K. H. Lockey, Journal of Experimental Biology **37,** 316 (1960).

76   B.-H. Kim, C.-H. Oh, K. Chun, T.-D. Chung, J.-W. Byun, and Y.-S. Lee, *A New Class of Surface Modifiers for Stiction Reduction*, 189 (IEEE Publications, Orlando, Florida, 1999).

77   R. Maboudian, W. R. Ashurst, and C. Carraro, Sensors and Actuators A: Physical **82,** 219 (2000).

78   C. Yang, U. Tartaglino, and B. N. J. Persson, Physical Review Letters **97,** 116103 (2006).

79   D. Ng, P. Y. Huang, Y. R. Jeng, and H. Liang, Electrochemical and Solid-State Letters **10,** H227 (2007).

80   D. Ng, S. Kundu, M. Kulkarni, and H. Liang, Journal of The Electrochemical Society **155,** H64 (2008).

81   P. C. Croghan and J. Noble-Nesbitt, Journal of Experimental Biology **143,** 537 (1989).

82   M. A. Willis and J. L. Avondet, Journal of Experimental Biology **208,** 721 (2005).

83   J. Boeckh, E. Priesner, D. Schneider, and M. Jacobson, Science **141,** 716 (1963).

84   R. Cooper, H. Lee, J. M. Gonzalez, J. Butler, S. B. Vinson, and H. Liang, Journal of Tribology **131,** 014502 (2009).

85   M. W. Holdgate and M. Seal, Journal of Experimental Biology **33,** 82 (1956).

86   B. Tang and A. H. W. Ngan, Soft Materials **2,** 183 (2004).

87   P. Angerer, W. Artner, E. Neubauer, L. G. Yu, and K. A. Khor, International Journal of Refractory Metals and Hard Materials **26,** 312 (2008).

88   M. Imafuku, H. Suzuki, K. Sueyoshi, K. Akita, and S.-i. Ohya, Applied Physics Letters **92,** 231903 (2008).

89   H. Suzuki, K. Akita, and H. Misawa, Japanese Journal of Applied Physics **42,** 2876 (2003).

90   A. K. Singh, H.-k. Mao, J. Shu, and R. J. Hemley, Physical Review Letters **80,** 2157 (1998).

91   J. Stoehr, in *Springer Series in Surface Sciences*, Berlin, Germany, 1992 (Springer-Verlag), p. 403.

92   H. Ade and H. Stoll, Nature Materials **8,** 281 (2009).

93   C. Wagner, W. Riggs, L. Davis, and J. Moulder, *Handbook of X-ray Photoelectron Spectroscopy* (Perkin Elmer Corporation, Eden Prairie, Minnesota, 1979).

94   R. Karazija, *Introduction to the Theory of X-ray and Electronic Spectra of Free Atoms* (Springer, New York, 1996).

95   F. Bach, *Front Matter* (Wiley-VCH Verlag, Weinheim, Germany, 2006).

96   D. Briggs and M. Seah, *Practical Surface Analysis* (Wiley, Chichester, England, 1990).

97   D. F. Ogletree, H. Bluhm, G. Lebedev, C. S. Fadley, Z. Hussain, and M. Salmeron, Review of Scientific Instruments **73,** 3872 (2002).

98   D. Y. Perera, Progress in Organic Coatings **28,** 21 (1996).

99   L. F. Francis, A. V. McCormick, D. M. Vaessen, and J. A. Payne, Journal of Materials Science **37,** 4717 (2002).

100   G. Jiang, W. Guan, and Q. Zheng, Wear **258,** 1625 (2005).

101   J. Jiang, F. Sheng, and F. Ren, Wear **217,** 35 (1998).

102   E. Kumacheva, Progress in Surface Science **58,** 75 (1998).

103   H. C. Meng and K. C. Ludema, Wear **181-183,** 443 (1995).

104   J. A. Williams, Wear **225,** 1 (1999).

105   D. Avnir, D. Farin, and P. Pfeifer, Journal of Colloid and Interface Science **103,** 112 (1985).

106   F. F. Ling, Wear **136,** 141 (1990).

107   M. Wakuda, Y. Yamauchi, S. Kanzaki, and Y. Yasuda, Wear **254,** 356 (2003).

108   B. Bharat, Journal of Vacuum Science & Technology B: Microelectronics and Nanometer Structures **21,** 2262 (2003).

[109] W. Townsend and J. Salisbury, Jr., in *IEEE International Conference on Robotics and Automation. Proceedings*, 883(IEEE Publications, Raleigh, North Carolina, 1987).

[110] T. Yamamoto, T. Yokohata, and Y. Kasamatsu, Magnetics, IEEE Transactions on **34,** 1753 (1998).

[111] C. Gu, D. W. Lynch, A. B. Yang, and C. G. Olson, Physical Review B **42,** 1526 (1990).

[112] H. Madhavaram, H. Idriss, S. Wendt, Y. D. Kim, M. Knapp, H. Over, J. Aßmann, E. Löffler, and M. Muhler, Journal of Catalysis **202,** 296 (2001).

[113] A. E. G. Cass, G. Davis, G. D. Francis, H. A. O. Hill, W. J. Aston, I. J. Higgins, E. V. Plotkin, L. D. L. Scott, and A. P. F. Turner, Analytical Chemistry **56,** 667 (1984).

[114] N. C. Foulds and C. R. Lowe, Analytical Chemistry **60,** 2473 (1988).

[115] R. R. Gagne, C. A. Koval, and G. C. Lisensky, Inorganic Chemistry **19,** 2854 (1980).

[116] J. F. Smalley, S. W. Feldberg, C. E. D. Chidsey, M. R. Linford, M. D. Newton, and Y.-P. Liu, Journal of Physical Chemistry **99,** 13141 (1995).

[117] M. Giorgetti, I. Ascone, M. Berrettoni, P. Conti, S. Zamponi, and R. Marassi, Journal of Biological Inorganic Chemistry **5,** 156 (2000).

[118] J. Kawai, H. Adachi, S. Hayakawa, S. Y. Zhen, K. Kobayashi, Y. Gohshi, K. Maeda, and Y. Kitajima, Spectrochimica Acta Part B: Atomic Spectroscopy **49,** 739 (1994).

[119] D. Ruzmetov, S. D. Senanayake, and S. Ramanathan, Physical Review B **75,** 195102 (2007).

[120] K. Amezawa, Y. Orikasa, T. Ina, A. Unemoto, M. Sase, H. Watanabe, T. Fukutsuka, T. Kawada, Y. Terada, and Y. Uchimoto, ECS Transactions **13,** 161 (2008).

[121] M. Ishii, K. Ozasa, and Y. Aoyagi, Microelectronic Engineering **67-68,** 955 (2003).

[122] B. Poumellec, F. Lagnel, J. F. Marucco, and B. Touzelin, physica status solidi (b) **133,** 371 (1986).

123   Y. Orikasa, T. Ina, T. Fukutsuka, K. Amezawa, T. Kawada, and Y. Uchimoto, ECS Transactions **13,** 201 (2008).

124   B. Poumellec, J. F. Marucco, and B. Touzelin, Physical Review B **35,** 2284 (1987).

125   A. Bianconi, M. Dell'Ariccia, P. J. Durham, and J. B. Pendry, Physical Review B **26,** 6502 (1982).

126   J. Wong, Materials Science and Engineering **80,** 107 (1986).

127   J. Wong, F. W. Lytle, R. P. Messmer, and D. H. Maylotte, Physical Review B **30,** 5596 (1984).

128   S. Nemat-Nasser, J. B. Isaacs, and M. Liu, Acta Materialia **46,** 1307 (1998).

129   L. Löffler and W. Mader, Journal of the European Ceramic Society **25,** 639 (2005).

130   W.-j. Huang and V. Ji, Transactions of Nonferrous Metals Society of China **16,** s735 (2006).

131   L. López-de-la-Torre, B. Winkler, J. Schreuer, K. Knorr, and M. Avalos-Borja, Solid State Communications **134,** 245 (2005).

132   P. J. Maudlin, S. I. Wright, U. F. Kocks, and M. S. Sahota, Acta Materialia **44,** 4027 (1996).

133   S. Chen and G. Gray, Metallurgical and Materials Transactions A **27,** 2994 (1996).

134   I. C. Noyan and J. B. Cohen., Crystal Research and Technology **24,** K37 (1989).

135   F. H. Featherston and J. R. Neighbours, Physical Review **130,** 1324 (1963).

136   O. Gülseren and R. E. Cohen, Physical Review B **65,** 064103 (2002).

137   J. Stringer, Oxidation of Metals **11,** 225 (1977).

138   K. Wang, Z. Liu, T. H. Cruz, M. Salmeron, and H. Liang, Journal of Physical Chemistry A **114,** 2489 (2010).

139   J. Zsakó, Journal of Thermal Analysis and Calorimetry **9,** 101 (1976).

140   A. K. Galwey, in *Advances in Catalysis* **26,** 247 (Academic Press, New York, 1977).

[141]   A. K. Galwey and M. E. Brown, Thermochimica Acta **300,** 107 (1997).

[142]   T. M. Adams and R. A. Layton, *Introductory MEMS: Fabrication and Applications*, 1st ed. (Springer, New York, 2009).

[143]   K. Geng, F. Yang, T. Druffel, and E. A. Grulke, Polymer **46,** 11768 (2005).

[144]   R. Schwaiger and O. Kraft, Journal of Materials Research **19,** 315 (2004).

[145]   T. Y. Tsui, C. A. Ross, and G. M. Pharr, in *Materials Research Society*, San Francisco, California, 1997 (Materials Research Society Symposia Proceedings), p. 57.

[146]   R. B. Beck and B. Majkusiak, Physica Status Solidi (a) **116,** 313 (1989).

[147]   V. Murali and S. P. Murarka, Journal of Applied Physics **60,** 4327 (1986).

[148]   F. Li, M. K. Balazs, and S. Anderson, Journal of The Electrochemical Society **152,** G669 (2005).

[149]   E. M. Young and W. A. Tiller, Applied Physics Letters **50,** 80 (1987).

[150]   S. M. Hu, Journal of Applied Physics **55,** 4095 (1984).

[151]   R. Beresford, Semiconductor Science and Technology **18,** 973 (2003).

[152]   M. Gad-el-Hak, *MEMS: Design and Fabrication*, 2nd ed. (CRC Press, Boca Raton, Florida, 2007).

[153]   B. Wong, A. Mittal, and Y. Cao, *Nano-CMOS Circuit and Physical Design* (Wiley-Interscience, Hoboken, New Yersey, 2004).

[154]   C. Wagner, in *American Society of Metalurgy*, (ASM Proceedings, Cleveland, Ohio, 1951).

[155]   B. E. Deal and A. S. Grove, Journal of Applied Physics **36,** 3770 (1965).

[156]   Y. Song, S. Dhar, L. C. Feldman, G. Chung, and J. R. Williams, Journal of Applied Physics **95,** 4953 (2004).

[157]   A. K. Galwey and M. E. Brown, Thermochimica Acta **386,** 91 (2002).

[158]   R. R. Razouk, M. E. Thomas, and S. L. Pressacco, Journal of Applied Physics **53,** 5342 (1982).

VITA

Rodrigo Alejandro Cooper was born in Mexico City, Mexico in 1983 and moved to Houston, TX in 1990. He completed his B.S. in Mechanical Engineering in 2006 at Texas A&M University while working as an undergraduate research assistant in the Surface Science group. He received his M.S. degree from Texas A&M University in 2008, only one and a half years after graduating from undergraduate studies. His studies on mechano-chemical alteration of materials began with his PhD studies within the same group. He received his doctorate in mechanical engineering on August 2011.

His permanent contact is:

Rodrigo Alejandro Cooper
Texas A&M University
Mechanical Engineering Dept.
MS 3123
College Station, TX 77843.

His email is rodrigocooper@gmail.com.